CO and CO_2 methanation over Ni catalysts supported on CeO_2, Al_2O_3 and Y_2O_3 oxides

C. Italiano[1], J. Llorca[2], L. Pino[1], M. Ferraro[1], V. Antonucci[1], A. Vita[1]

[1]*CNR-ITAE, Institute for Advanced Energy Technologies "Nicola Giordano", Via S. Lucia sopra Contesse 5, 98126 Messina, Italy*

[2]*Institute of Energy Technologies, Department of Chemical Engineering and Barcelona Research Center in Multiscale Science and Engineering. Universitat Politècnica de Catalunya, EEBE, Eduard Maristany 10-14, 08019 Barcelona, Spain*

Abstract

In this paper, the methanation of carbon oxides (CO and CO_2) was studied as an interesting way to provide a renewable energy source of synthetic natural gas (SNG) simultaneously reducing the emission of greenhouse gases. 15 wt.% Ni-based catalysts supported on CeO_2, Al_2O_3 and Y_2O_3 oxides were synthesized by solution combustion synthesis. Then, a second series on Ni/Y_2O_3 catalysts was prepared with different Ni loading (7-35 wt.%). The physicochemical properties of the catalysts were characterized by N_2-physisorption, XRD, H_2-TPR, CO-chemisorption, TEM, UV-Vis DRS, XPS, and CO_2-TPD. The effect of reaction temperature (250-500°C) was investigated under atmospheric pressure, space velocity (GHSV) of 10,000 h^{-1}, and stoichiometric reactants ratio of $(H_2\text{-}CO_2)/(CO+CO_2) = 3$. A 200 h stability test was also carried out at 350°C over the 25 wt.% Ni/Y_2O_3 catalyst.

It can be concluded that the nature of Ni-support interactions played a crucial role in enhancing CO and CO_2 hydrogenation at relatively low reaction temperature. Ni/CeO_2 catalyst deactivated rapidly due to coke deposition, while the formation of $NiAl_2O_4$ spinel was the main reason of the lower activity of the Al_2O_3-supported system. Activity data for Ni/Y_2O_3 catalysts were closely related to the degree of Ni dispersion as well as to the medium-strength basicity. Good anti-coking and anti-sintering ability were observed after 200 h of lifetime test over the $25Ni/Y_2O_3$ catalyst.

Keywords

CO and CO_2 methanation; Ni catalysts; Support effect; Ni/Y_2O_3; SNG production.

1. Introduction

Power-to-Gas (P2G) technologies could play an important role in future energy scenario in improving the security of energy supply while reducing the emission of greenhouse gases [1,2]. The P2G pathway consists of two main steps: i) electrolysis of water to produce hydrogen by using the excess renewable electricity from fluctuating renewable sources and ii) hydrogenation of carbon oxides (CO and/or CO_2), otherwise known as syngas methanation, to produce Synthetic Natural Gas (SNG) [3]. Firstly reported by Sabatier and Senderens in 1902 [4], the interest to the syngas methanation has remarkably grown over the past decade as a practical method for carbon dioxide reduction and a tool for natural gas production whose consumption increases by 1.6% per year since 2008 [5,6]. Indeed, methane is an important energy source in both manufacturing and transport applications, due to existing distribution infrastructure and high energy density [7,8]. Methanation reactions of syngas proceed according to:

$$CO + 3H_2 \rightleftarrows CH_4 + H_2O, \qquad \Delta H^0_{298K} = -206 \text{ kJ mol}^{-1} \qquad (1)$$

$$CO_2 + 4H_2 \rightleftarrows CH_4 + 2H_2O, \qquad \Delta H^0_{298K} = -165 \text{ kJ mol}^{-1} \qquad (2)$$

Actually, the high price of natural gas is becoming a cause for concern in some countries heavily dependent on imports [9]. Thus, new pathways for SNG production have been intensively studied, including the syngas methanation from biomass and coal gasification plants [10]. Syngas methanation can be applied to consume the Blast Furnace Gas (BFG) and the Coke Oven Gas (COG) alleviating the negative environmental impact of carbon-intensive industries[11,12]. In addition, these reactions can also been used to remove trace amounts of CO from the feed gas for ammonia synthesis as well as from the reformed gas for polymer electrolyte membrane fuel cells [13].

Reactions (1) and (2) are highly exothermic and thermodynamically favored at low temperature (< 400°C) [14]. Moreover, the large reaction heat accumulates and causes severe hotspots in the reactor thereby shortening the catalysts' life-time [15,16]. Thus, extensive studies have been conducted to develop methanation catalysts with high activity at low temperature and enhanced anti-sintering and anti-coking properties [14,17]. Many metals, such as Ru, Ni, Fe, Co, Mo, Rh, have been used to catalyze methanation reactions [18–20]. Although Ru is the most active metal, limited resource and high cost limit the large-scale commercialization of Ru-based catalysts. Contrarily, Ni-based systems are more attractive for CO_x methanation to SNG because of their low cost and high selectivity to methane [21,22]. However, their stability is often compromised by deactivation due to sintering and carbon occurring under different operating conditions [23]. In particular, the carbon deposition phenomenon occurs either through CO disproportionation reaction (3) or via CH_4 decomposition (4) [24]:

$$2CO \rightarrow C + CO_2, \qquad \Delta H^0_{298K} = -173 \text{ kJ mol}^{-1} \qquad (3)$$

$$CH_4 \rightarrow C + 2\,H_2, \qquad \Delta H^0_{298K} = 75 \text{ kJ mol}^{-1} \qquad (4).$$

Thus, several supports including Al_2O_3 [5,9,23,25], SiO_2 [13,14,26], TiO_2 [13,25,27], ZrO_2 [9,28,29] and CeO_2 [13,17,26,30] have been studied to improve the activity and long-time stability of Ni-based catalysts. Considerable efforts have been also devoted to elucidate the effect of Ni-support interactions as well as the bonding and reactivity of chemisorbed species [9,23,31]. However, the activity and selectivity data for CO_2 methanation are markedly different from those for CO methanation [29,32]. As an example, Al Le and co-workers [13] investigated the catalytic performance for CO methanation, showing the following activity order: $Ni/CeO_2 > Ni/ZrO_2 > Ni/TiO_2 > Ni/SiO_2 > Ni/\gamma\text{-}Al_2O_3$. The highest activity of Ni/CeO_2 was ascribed to the smallest Ni particles whereas the formation of $NiAl_2O_4$ resulted in decreasing the amount of active Ni specie, lowering the performance of the $Ni/\gamma\text{-}Al_2O_3$ catalyst. Interestingly, Zhao et al. [5] showed that the activity for CO methanation over Ni/Al_2O_3 catalyst was sensitive to Ni particle size. In this study, Ni particles with relatively large diameters were effective for the syngas methanation, simultaneously showing high activity and anti-CO-poisoning ability. Muroyama et al. [33] studied the CO_2 methanation over Ni supported catalysts. The following order of CH_4 yield at 250°C, $Ni/Y_2O_3 > Ni/Sm_2O_3 > Ni/ZrO_2 > Ni/CeO_2 > Ni/Al_2O_3 > Ni/La_2O_3$, was mainly attributed to the basic property of the catalysts. In addition, the utilization of Y_2O_3 as catalytic support for several applications including reforming processes, selective reduction of NO_x, etc., was widely investigated in literature [34–37]. Instead, to the best of our knowledge, only few papers [33,38] studied the activity of Y_2O_3-supported catalysts towards methanation reactions for the production of SNG. In the work of Yan et al. [38], the moderate $Ni\text{-}Y_2O_3$ interaction resulted in a superior activity for CO_2 methanation as well as a robust stability in CO-containing reaction mixtures.

In this study, 15 wt.% Ni-based catalysts supported on CeO_2, Al_2O_3, and Y_2O_3 oxides were synthesized by solution combustion synthesis (SCS). Among them, Y_2O_3 was selected as the best catalytic support and, therefore, a second series of Ni/Y_2O_3 catalysts containing different Ni loading (7-35 wt.%) was prepared. The physicochemical properties of the synthesized catalysts were determined by N_2-physisorption, XRD, H_2-TPR, CO-chemisorption, TEM, UV-Vis DRS, XPS, and CO_2-TPD. The methanation of CO and CO_2 was investigated under atmospheric pressure, in the temperature range of 250-500°C, at constant gas hourly space velocity (GHSV) of 10,000 h^{-1}, and stoichiometric reactants ratio of $(H_2\text{-}CO_2)/(CO+CO_2) = 3$. A stability test over 200 h of time-on-stream was also performed over the 25 wt.% Ni/Y_2O_3 catalyst. A comprehensive understanding of the degree of Ni dispersion and the strength of Ni-support interaction as well as the basic properties was provided to optimally design an effective catalyst for the production of SNG via CO and CO_2 methanation.

2. Experimental

2.1. Catalysts preparation

High-purity reagent-grade were purchased from Sigma-Aldrich and used as received: $Ni(NO_3)_3 \cdot 6H_2O$, $Ce(NO_3)_3 \cdot 6H_2O$, $Y(NO_3)_3 \cdot 6H_2O$, and $Al(NO_3)_3 \cdot 9H_2O$ were used as metal precursors, while urea (CH_4N_2O) was used as fuel. Ni-based catalysts were synthesized by the solution combustion synthesis (SCS) method as previously described [39,40]. Briefly, stoichiometric amounts of metal precursors and urea were dissolved in the minimum quantity of distilled water under magnetically stirring to obtain a clear solution, which was then transferred to a muffle furnace heated at 350°C. After water evaporation, self-ignition and combustion occurred with rapid increase in temperature and gas evolution (N_2, CO_2, H_2O), yielding a voluminous powder. The resulting powder was calcined in static air furnace at 600°C (heating rate of $5°C \cdot min^{-1}$) for 2 h. Ni-based catalysts supported on CeO_2, Al_2O_3, and Y_2O_3 oxides were synthesized at fixed Ni loading of 15 wt.%. Then, a second series of Ni/Y_2O_3 catalysts containing different Ni loading (7-35 wt.%) was synthesized. For comparison, Y_2O_3 support was also prepared by the same SCS method. The Ni content in the catalytic powders was determined by chemical analysis (ICP/OES) and the results are summarized in Table 1, where the main physico-chemical features of the synthesized systems are also reported.

2.2. Catalysts characterization

N_2 adsorption-desorption isotherms were recorded on a *Micromeritics ASAP 2020* instrument at liquid nitrogen temperature (-196°C). Specific surface area (SA_{BET}) and pore volume (PV_{BJH}) were estimated using the Brunauer-Emmet-Teller (BET) and Barett-Joyner-Halenda (BJH) equations, respectively. The pore size distribution was calculated by the density functional theory (DFT) method. Prior to measurements the samples were degassed under high vacuum for 6 h at 300°C.

X-ray diffraction (XRD) analysis was performed on a *Philips X-Pert 3710* diffractometer with a Cu-Kα monochromatized radiation source ($\lambda = 1.5406$ Å) at 40 kV and 20 mA. Continuous scans were collected with a scan rate of $1.50° \cdot min^{-1}$ within the range $15° < 2\theta < 75°$, while a scan rate of $0.06° \cdot min^{-1}$ was applied to highlight the Y_2O_3 (222) reflection ($28° < 2\theta < 31°$). The peaks were assigned according to the PCPFWIN database. The CeO_2 and Y_2O_3 crystallite sizes were calculated by the Scherrer equation on the main CeO_2 (111) and Y_2O_3 (222) reflection peaks.

H_2 temperature-programmed reduction (H_2-TPR) and CO_2 temperature-programmed desorption (CO_2-TPD) were performed on a *Micromeritics ChemiSorb 2750* instrument equipped with a thermalconductivity (TCD) detector. In a typical H_2-TPR test, the as-calcined catalyst was reduced by a 5% H_2/Ar gas mixture ($30\ NmL \cdot min^{-1}$) while the temperature was increased from room temperature to 1000°C at a rate of $20°C \cdot min^{-1}$. The hydrogen consumption was determined based on the H_2-TPR patterns of known amounts of CuO.

In CO_2-TPD experiments, the sample was reduced in 50% H_2/N_2 flow (40 NmL·min^{-1}) at 600°C for 60 min, cooled to room temperature under He flow (30 NmL·min^{-1}) and exposed to CO_2 stream (30 NmL·min^{-1}) for 30 min. The physisorbed CO_2 was removed by He purging at room temperature for 1 h. Then, the temperature was increased up to 600°C at a rate of 10°C·min^{-1} under He flow (30 NmL·min^{-1}) and the desorbed CO_2 was monitored by TCD, which was previously calibrated by injections of pure CO_2 pulses.

CO-chemisorption measurements were performed at room temperature on the same instrument. Before chemisorption, the sample was reduced in 50% H_2/N_2 gas mixture (40 NmL·min^{-1}) at 600°C for 60 min. Then, the following standard procedure was applied at room temperature: i) oxidation in O_2 flow (30 Nml·min^{-1}) for 15 min; ii) treatment in CO_2 flow (30 Nml·min^{-1}) for 15 min; iii) reduction in H_2 flow (30 Nml·min^{-1}) for 30 min. Finally, a mixture of 10% CO in He was injected in pulses of 600 μL each until the fulfilment of constant outlet peaks. The Ni dispersion (D_{Ni}) was calculated from the ratio between the number of surface Ni atoms (Ni_s) and the total number of Ni atoms (Ni_t). by the equation [8]:

$$D_{Ni}(\%) = \frac{Ni_s}{Ni_t} \cdot 100 = \frac{f_{CO/Ni} \cdot V_{CO} \cdot M_{Ni}}{22414 \cdot L_{Ni} \cdot d_r} \cdot 100 \qquad (5)$$

where $f_{CO/Rh}$ (=1) is the stoichiometric factor for CO chemisorption, V_{CO} (cm$^3_{STP}$·g^{-1}) is the amount of CO chemisorbed on Ni, M_{Ni} (=58.69 g·mol^{-1}) is the molar mass of Ni, L_{Ni} is the Ni content in the catalyst, and d_r is the reduction degree of Ni calculated from H_2-TPR.

Transmission electron microscopy (TEM) micrographs were obtained using a *Philips CM12* instrument. The reduced samples were subjected to ultrasonic irradiation in isopropyl alcohol and dispersed on holey-carbon copper grids.

The UV–Vis diffuse reflectance spectroscopy (UV-Vis DRS) was carried out using a *Agilent Cary Series UV–vis-NIR* spectrophotometer equipped with an integrating sphere diffuse reflectance accessory. The powders materials were mounted in an appropriate quartz cell which provided an “infinite” sample thickness and the spectra were recorded at room temperature in the wavelength range of 200–800 nm. Barium sulphate was used as the reference spectra. The spectra are presented in form of the Kubelka-Munk function being defined as $F(R) = (1–R)^2/(2R)$ with $R = R_s/R_r$, where R_s is the reflectance of the sample and R_r is the reflectance of $BaSO_4$. Energy gap (E_g) values were estimated from the Tauc relation, i.e. $[F(R)·h·v]^n = B\ (h·v – E_g)$, where *B* is a constant of proportionality, *h* is Plank’s constant, *v* is the frequency, and *n* is 2 for direct allowed transitions.

X-ray photoelectron spectroscopy (XPS) was conducted on a *SPECS* system equipped with a *XR50* source operating at 150 W and a *Phoibos 150 MCD-9* detector. The analysis chamber was maintained at a pressure always below 10^{-7} Pa. The binding energy (BE) values were measured with pass energy of 25 eV and energy step of 0.1 eV. All the spectra were referenced to the C1s line at 284.8 eV from the adventitious carbon. Quantification of surface composition was based on the peak fitting and normalization of Ni (2p 3/2), Al (2p), Y (3d 5/2), and Ce (3d 5/2) primary peaks.

2.3. CO and CO_2 methanation

Catalytic tests were carried out at atmospheric pressure in a fixed-bed quartz reactor (0.6 cm inner diameter, 25 cm length). Typically, 0.1 g of catalyst (50-70 mesh) was diluted with 0.2 g of inert quartz (with same pellets size) to distribute the heat produced by the reaction along the reactor axis and to prevent hot-spot phenomena. The resulting catalytic bed (length ≈ 1 cm) was placed at the centre of the quartz tube horizontally placed inside a furnace. Prior to reaction, the catalysts were *in-situ* reduced under 50% H_2/N_2 gas mixture (40 $NmL \cdot min^{-1}$) at 600°C for 1 h. The total gas flow rate (50 cm^3 min^{-1}) was introduced into the reactor by mass flow controllers (*Brooks Instrument Smart Mass Flow*) at a gas hourly space velocity (GHSV) of 10,000 h^{-1}. The feed consisted in 4.9% CO, 6.1% CO_2, 39.0% H_2, and N_2 as balance gas, which corresponded to a stoichiometric reactants ratio of $(H_2\text{-}CO_2)/(CO+CO_2) = 3$.

The activity tests were conducted by increasing the temperature from 250 to 500°C (with 50°C of increasing step) and back (300°C) to verify stable catalyst conditions during these measurements. The durability of the 25 wt.% Ni/Y_2O_3 catalyst was also evaluated at 350°C for 200 h of time-on-stream. The reaction temperature was regulated by a chromel/alumel thermocouple located at the center of the catalytic bed. Moreover, two thermocouples were positioned at the inlet and at the outlet of the catalytic bed to measure the gradient temperature generated by reactions.

Reagent and product mixtures were analyzed online by gas chromatograph (*Agilent 6890 Plus*) equipped with thermal conductivity detector (TCD) and flame ionization detector (FID). The analysis were collected every 20 min after 1 h of steady-state operation at each temperature. N_2 was used as internal standard for mass balance calibration. CO_2 conversion (χ_{CO_2}), CO conversion (χ_{CO}), and CH_4 yield (Y_{CH_4}) were defined as follows:

$$\chi_{CO_2}(\%) = \frac{F_{CO_2,in} - F_{CO_2,out}}{F_{CO_2,in}} \cdot 100 \tag{6}$$

$$\chi_{CO}(\%) = \frac{F_{CO,in} - F_{CO,out}}{F_{CO,in}} \cdot 100 \tag{7}$$

$$Y_{CH_4}(\%) = \frac{F_{CH_4,out}}{F_{CO,in} + F_{CO_2,in}} \cdot 100 \tag{8}$$

where $F_{i,in}$ and $F_{i,out}$ are the inlet and outlet flow ($mol \cdot s^{-1}$) of i species, respectively. Carbon balance was always close to 100±0.5%. The experimental results were compared with the thermodynamic equilibrium values calculated by a commercial steady-state simulation package named HSC Chemistry 7.1®, based on the minimization of Gibbs free-energy. The intrinsic CO_2 methanation rate, expressed as moles of CO_2 consumed per unit mass of nickel per second (r_{CO_2}, $mol \cdot g^{-1} \cdot s^{-1}$), was calculated by using the following equation [41]:

$$r_{CO_2} = \frac{F_{CO_2,in} \cdot X_{CO_2}}{W \cdot L_{Ni}} \tag{9}$$

where W is the catalyst weight (g). The turnover frequency of CO_2 conversion (TOF_{CO_2}), defined as moles of CO_2 converted per moles of surface Ni atom per second (s^{-1}), was defined as follows [41]:

$$TOF_{CO_2} = \frac{F_{CO_2,in} \cdot X_{CO_2}}{Ni_S} \tag{10}$$

where the number of surface Ni sites (Ni_s) was calculated based on the CO-chemisorption results.

3. Results and discussion

3.1. Catalysts characterization

3.1.1. N_2 adsorption-desorption

Figure 1 shows the N_2 adsorption-desorption isotherms and the corresponding pore size distribution of the as-synthesized catalysts, while the detailed textural parameters are listed in Table 1. It is seen from Figure 1a that the isotherm of $15Ni/Al_2O_3$ sample displayed classic IV type curve (IUPAC), corresponding to the typical feature of mesoporous materials [42,43]. The apparent H2 hysteresis loop was associated to capillary condensation taking place in mesopores with neck-bottle shaped, while the sharp rise at low relative pressure ($p/p0 \approx 0.4$) indicated a high specific surface area (250.4 $m^2 \cdot g^{-1}$) [42,44,45]. Besides, a narrow pore size distribution was evidenced in Figure 1b, corresponding to an Average Pore Diameter (APD) of 4.9 nm (Table 1). Differently, mesoporous Ni/CeO_2 and Ni/Y_2O_3 catalysts showed H3 type hysteresis loop, characteristic of plate-type particles with slit-shaped pores [46–49]. In addition, the appearance of hysteresis loop at high relative pressure ($p/p0 > 0.6$) was indicative of a broad pore size distribution, containing both accessible mesopores and macropores in the structure (Figure 1b) [50,51] Therefore, lower surface area and higher APD values were calculated for Ni/CeO_2 (20.6 $m^2 \cdot g^{-1}$, 12.6 nm) and Ni/Y_2O_3 (19.3 $m^2 \cdot g^{-1}$, 30.3 nm) systems.

It was seen that there was no specific trend for textural features with increasing in Ni content (Figures 1c,d). The maximum BET surface area (40.7 $m^2 \cdot g$-1) was observed for the catalyst containing 7 wt.% of Ni, slightly higher than the corresponding Y_2O_3 support (35.9 m2·g-1), mainly due to the lower flame temperature achieved during the combustion reaction [52]. However, the decrease in specific surface area (19.3-26.9 m2·g-1) by further increasing the Ni loading (15-35 wt.%) could be attributed to pores filling by Ni species [51,53].

3.1.2. XRD

Figure 2 shows the the XRD patterns of the as-prepared Ni-based catalysts supported on CeO_2, Al_2O_3, and Y_2O_3 oxides. Ni/CeO_2 catalyst showed the diffraction peaks of cerium oxide (JCPDS 4-593) and nickel oxide (JCPDS 4-835) cubic structures. The calculated unit cell parameter (0.538 nm, Table 1) was lower than the lattice parameter of the bulk CeO_2 (0.541 nm, JCPDS 4-593), accounting for the shrinkage of the CeO_2 cell due to the partial substitution of Ce^{4+} (0.097 nm) with smaller Ni^{2+} (0.081 nm) cations [54,55]. In addition, the CeO_2 average crystallite size, calculated from the Scherrer equation on the main CeO_2 (111) reflection ($2\theta = 28.55$), was 10.4 nm (Table 1).

Spinel nickel-aluminate phase ($NiAl_2O_4$) at diffraction lines $2\theta = 19.07°$, 31.41°, 37.01°, 44.99°, 59.68°, and 65.54° (JCPDS 10-339) was revealed for the $15Ni/Al_2O_3$ catalyst (Figure 2). Moreover, the presence of weak broad peaks suggested a predominantly amorphous nature of the $NiAl_2O_4$ phase [56].

$15Ni/Y_2O_3$ catalyst showed the characteristic peaks at $2\theta = 20.45°$, 29.16°, 33.77°, 35.89°, 39.84°, 43.47°, 48.54°, and 57.59° (Figure 2) which could be indexed to (211), (222), (400), (411), (332), (431), (440), and (310) crystal planes of cubic Y_2O_3 (JCPDS 25-1200) [57,58]. In addition, very weak signals of NiO crystallytes (JCPDS 4-835) revealed well-dispersed NiO particles on the Y_2O_3 support. However, the intensity of the NiO diffraction peaks increased with increasing the Ni loading, as evidenced in Figure 3a. Thus, a partial aggregation of the dispersed NiO species occurred on the surface of the mesoporous Y_2O_3 support at higher Ni loading (Figure 3a). Furthermore, the Y_2O_3 reflections of the Ni-based catalysts were slightly shifted to higher degrees with respect to those of bare Y_2O_3 support (Figure 3b), which was attributed to the lattice contraction induced by Ni addition. Indeed, the partial substitution of Y^{3+} (0.102 nm) with smaller Ni^{2+} (0.081 nm) cations led to the shrinkage of the Y_2O_3 cell. It was confirmed by the calculated unit cell parameters (1.057-1.058 nm, Table 1) lower than the lattice parameter of the Y_2O_3 support (1.060 nm, Table 1). Additionally, Y_2O_3 crystallites comprised between 8.8 and 13.5 nm were calculated by the Scherrer's equation on the main Y_2O_3 (222) diffraction peak (Table 1). After reducing the catalyst, additional diffraction peaks were observed at $2\theta = 44.50°$ and 51.84° (Figure 3c), corresponding to the (111) and (200) planes of metallic Ni, respectively (JCPDS 4-850) [59]. The intensity of the Ni peaks increased by increasing the Ni loading, which just corresponded to the above-identified fact that the catalyst had less dispersed Ni particles. Moreover, the coexistence of both Ni and NiO phases in the reduced $35Ni/Y_2O_3$ catalyst indicated that the Ni metal phase was not totally reduced under the adopted conditions [59]. It is quite interesting to note that there was no difference in the crystal structure of Y_2O_3 phase after the reduction treatment, indicating the high resistance to sintering during the reduction step. Therefore, the calculated Y_2O_3 crystallites of the reduced systems (11.9-13.5) were only slightly larger than those of the corresponding calcined catalysts (Table 1).

3.1.3. H_2-TPR and CO-Chemisorption

The reducibility of the synthesized samples was studied by H_2-TPR and the results are displayed in Figure 4. The TPR profile of the 15Ni/Al_2O_3 catalyst (Figure 4a) had a broad reduction peak with maximum at ca. 770°C ascribed to the reduction of $NiAl_2O_4$ spinel, which is strongly bonded to the support and hard to be reduced [60–62]. Therefore, Ni species in 15Ni/Al_2O_3 catalyst were almost not reduced into Ni metal under the experimental conditions adopted in this study.

Reduction of 15Ni/CeO_2 system (Figure 5a) showed four peaks at ca. 270, 350, 440 and 850°C, as previously reported [63]. The low-temperature peak at ca. 270°C was ascribed to the reduction of adsorbed oxygen on the Ni-Ce mixed oxide [64]. The peak at ca. 350 was attributed to the reduction of dispersed NiO interacting with (but not chemically bound to) the support, while the peak at ca. 440°C was ascribed to the formation of Ni-Ce-O_x solid solution, in agreement with XRD results (Table 1). Moreover, contribute of different sized Ni species which are reducible at different temperatures cannot be excluded [65]. Finally, the high-temperature peak at ca. 850°C was due to the CeO_2 bulk reduction [63]. The experimental hydrogen consumption and the relative reducibility of the synthesized samples are summarized in Table 2. Quantitative TPR analysis was performed from ambient temperature up to 600°C (experimental reduction temperature before catalytic tests). The calculated hydrogen consumption (13.16 $mmol_{H2}/g_{NiO}$) was almost equal to the H_2 theoretical quantity, leading to a reduction degree of 98.3% (Table 2).

The TPR profiles of Ni/Y_2O_3 catalysts (Figure 4b) showed multiple reduction peaks. The low temperature peak (at ca. 200-245°C) was due to the reduction of NiO-promoted oxygen vacancies on Y_2O_3, while the medium (at ca. 410-460 °C) and high temperature (at ca. 500-540°C) peaks could be attributed to the reduction of bulk NiO species with different extent interactions with the support [52,66]. The TPR profile of bare Y_2O_3 support is also reported, showing a very weak reduction peak due to the lattice oxygen on its surface [36,66]. Generally, the reduction of bulk NiO (not reported) occurs in the temperature range of 280-300°C [67]. Therefore, the shift to higher temperature suggested the presence of strong Ni-support interactions [67–69]. As reported by Singha et al. [65], different sized particles are reducible at different temperatures. Indeed, the reduction of larger NiO particles required more time and temperature, resulting in a broad reduction pattern [65,70]. Therefore, it could be speculated that the peak at 410 and 510°C was due to the reduction of highly disperded and agglomerated NiO particles, respectively (7Ni/Y_2O_3). With increasing Ni loading, the high temperature peak increased in intensity and shifted towards higher temperature (Figure 4b), as larger NiO crystals were not easily reduced, in accordance with XRD (Figure 3) evidences [71,72]. Moreover, the reducibility of the catalysts decreased with increasing the Ni loading from 99.3% (7Ni/Y_2O_3) to 81.0% (35Ni/Y_2O_3), because larger Ni oxide particles was not readily exposed to hydrogen for reduction.

Metal dispersion (D_{Ni}) of the catalysts was also measured and compared. It is observed that Ni dispersion decreased with increasing the Ni loading due to agglomeration of metal particles. Indeed, the dispersion values followed the order $7Ni/Y_2O_3$ (10.0%) > $15Ni/Y_2O_3$ (8.7%) > $25Ni/Y_2O_3$ (7.3%) > $35Ni/Y_2O_3$ (4.1%) (Table 1).

3.1.4. TEM

TEM images of the Ni-based catalysts are shown in Figure 5. The average particle size (PS_{Ni}) were determined by analyzing the data from different TEM images and summarized in Table 1. Agglomerated catalyst particles were observed in the $15Ni/CeO_2$ system (Figure 5a), which was the main reason for low Ni dispersion (5.2%, Table 1). Contrarily, the Ni particles were widely dispersed in the Al_2O_3 support (Figure 5b). Besides, Ni species appeared to be of spherical morphology with a mean size of ca. 9 nm (Table 1). Well-dispersed Ni particles of ca. 11-12 nm were measured over the $15Ni/Y_2O_3$ (Figure 5c) and $25Ni/Y_2O_3$ (Figure 5d) catalysts. As shown in Figure 5e, darker area were attributed to metallic Ni particles, showing fringes with d-spacing of 0.2 nm due to the (111) planes of Ni. In addition, fringes with d-spacing of 0.3 and 0.4 nm were attributed to the (222) and (211) planes of cubic Y_2O_3, respectively. Instead, agglomerated Ni particles were clearly observed over the $35Ni/Y_2O_3$ catalyst (Figure 5f).

3.1.5. UV-Vis DRS

Figure 6 shows the UV-Vis reflectance spectra of the as-prepared Ni/Y_2O_3 catalysts with different Ni loading (7-35 wt.%); the absorption spectrum of the corresponding support (Y_2O_3) is also shown for comparison. All samples presented similar profiles with different excitation regions. The first band between 200 and 220 nm could be assigned to the adsorption of Y_2O_3, i.e. the electron transfer from the 2p orbitals of O^{2-} (valence band) to the 5s4d orbitals of Y^{3+} (conduction band) [73]. The second band, localized between 220 and 300 nm was attributed to $O^{2-} \rightarrow Ni^{2+}$ change transfer band, i.e. transition from 2p orbitals of O^{2-} (valence band) to 3d orbitals of Ni^{2+} (conduction band). As fringerprints for NiO, the weak band in the 400-800 nm range was ascribed to d-d transitions of octhaedreal Ni^{2+} [74,75]. In addition, the red shift (higher wavelength) in the change transfer band (Figure 6a) can be attributed to the formation of defect levels due to the doping with transition metal ions [73,76,77].

The band gap energies were determined by using the intercept of the tangent to the graph (Tauc's plot), obtained by plotting the square root of the Kubelka-Munk function multiplied by the photon energy $[F(R)\cdot h\cdot \nu]^2$ versus the photon Energy ($h\cdot\nu$), as shown in Figures 6b and 6c. The estimated band gap for the Y_2O_3 support was consistent with the reported band gap of cubic Y_2O_3 (5.78 eV) [78,79]. A decreased band energy gap was calculated for the $7Ni/Y_2O_3$ catalyst (5.65 eV), attributed to the structural changes caused by the formation of Ni-Y-O_x solid solutions [76,80], in agreement with XRD results (Figure 3, Table 1). Indeed, the incorporation of interstitial nickel in the lattice of Y_2O_3 support generated novel energetic level in the interband gap, leading to a reduction in the band gap of the metal oxide [81,82].

A further decrease in the band gap values was observed by increasing the Ni loading, following the order $15Ni/Y_2O_3$ (5.53 eV) < $25Ni/Y_2O_3$ (5.01 eV) < $35Ni/Y_2O_3$ (3.99 eV). As previously reported [83,84], Ni species size can affect the band gap, since the bigger the particles, the higher the amounts of defects able to generate intermediate energy level distribution within the band gap. Indeed, the results obtained in this study clearly indicated that the band-gap was inversely proportional to the Ni size determined by CO-chemisorption (Table 1).

3.1.6. XPS

Figure 7 presents the recorded binding energies (BE) of the Ni $2p_{3/2}$ core level spectra of the as-prepared and used catalysts. From integration of XPS spectra, the surface distribution of Ni species was calculated and data are summarized in Table 3. First, Ni $2p_{3/2}$ region of the as-prepared $15Ni/Al_2O_3$ catalyst (Figure 7a) revealed a main peak at BE ≈ 854.5 eV together with a broad shake-up satellite peak at BE ≈ 861 eV. The main peak at lowest binding energy could be assigned to Ni^{2+} species interacting strongly with alumina as $NiAl_2O_4$ like structure formed on the Ni/Al catalyst [85,86]. It should be noticed that an almost equal spectrum was recorded for the post-reacted $15Ni/Al_2O_3$ system (after the in-situ reduction treatment and catalytic test), further confirming the strong metal-to-support interactions due to the formation of stoichiometric $NiAl_2O_4$ spinel [87]. Moreover, no peak corresponding to reduced nickel (Ni^0) was detected (Figure 7a), suggesting that Ni species were not reduced under the adopted conditions, in agreement with TPR results.

The Ni $2p_{3/2}$ XPS spectra of the as-prepared $15Ni/CeO_2$ catalyst (Figure 7b) revealed two adjacent bands with maximum at BE ≈ 854 eV and BE ≈ 855.5 eV, labelled as Ni(II) and Ni(II)*, together with a broad satellite peak at BE ≈ 861 eV, consistent with the presence of Ni^{2+} species [88–90]. This double peaked structure suggested the presence of surface Ni species with different environments [91]. In particular, the peak at highest binding energy (Ni(II)) was ascribed to presence of NiO highly dispersed on the support surface which created higher metal-support interaction. Instead, the second feature on the low binding-energy side (Ni(II)*) belonged to bigger NiO particles, being their photoemission affected by the presence of Ni cations as next-nearest neighbours [92]. Moreover, from the relative surface concentration of Ni^{2+} species (Table 3) it could be seen that most of Ni element existed in the form of extended particles of NiO (Ni(II)* = 63 at.%). The XPS of the post-reacted samples (Figure 7b) clearly showed the co-existence of Ni^{2+} and metallic Ni^0 (peak at BE ≈ 251.5 eV). However, TPR analysis indicated a complete NiO reduction at 600°C

(Figure 5, Table 2). Therefore, the presence of Ni^{2+} could be due to exposure of metallic Ni to air during the sampling for measurements.

The $Ni2p_{3/2}$ spectrum in Figure 7c consisted of a double peaked structure (BE ≈ 854 eV and BE ≈ 855.5 eV) and a shakeup satellite peak at ≈861.0 eV, ascribed to the presence of NiO species with different size on the surface of the as-prepared Ni/Y_2O_3 catalysts. As the Ni content increased from 7 to 35 wt.%, the atomic fraction of the Ni(II)* species (at BE ≈ 854 eV) increased from 33 to 73%, due to the presence of larger NiO crystals [74]. Moreover, the intensity shake-up satellite also increased with Ni loading, accounting for the partial aggregation of dispersed NiO particles occurring on the surface of Y_2O_3 support [60,93]. This observation agrees with CO-chemisorption (Table 1) and TPR measurements (Figure 4). After reaction, the XPS pattern of the $15/Y_2O_3$ and $25Ni/Y_2O_3$ catalysts changed (Figure 7d), showing a new bands at lower binding energy (BE ≈ 852 eV), which corresponded to metallic Ni^0 species. The amount of metallic nickel slightly increased with Ni content and time-on-stream (Table 3). Thus, 32% of Ni^0 was calculated over the post-reacted $15Ni/Y_2O_3$, which increased to 35% and 39% over the $25Ni/Y_2O_3$ after activity test and 200 h stability test, respectively (Table 3). The presence of the NiO species could be due to the incomplete reduction of NiO, in agreement with TPR results [94]. However, partial surface oxidation of metallic Ni to air during sample manipulation can not be excluded. For the sake of clarity, the Auger LVV band was also recorded (see inset in Figure 7d) and the characteristic profile at 640-641 eV of metallic nickel was visible in the post-reacted $25Ni/Y_2O_3$ samples.

3.1.7. CO_2-TPD

The TPD results after CO_2 adsorption on freshly reduced catalysts are shown in Figure 8. The corresponding values for the CO_2 uptake are given in Table 4. Three Lewis alkaline sites were identified, namely weak (<150°C), moderate (150-450°C) and strong (>450°C), depending on the desorption temperature of CO_2 [95]. $15Ni/CeO_2$ catalyst scarcely possessed basic sites, exhibiting only small amounts of desorbed CO_2 in the low- and high-temperature regions (Figure 8a) [26,33,96]. A large amount of desorbed CO_2 (315.92 $\mu mol_{CO2}\cdot g^{-1}$) was observed in the wide temperature range for $15Ni/Al_2O_3$, mainly due to the high surface area of this material (250.4 $m^2\cdot g^{-1}$) [33]. However, poor strongly-adsorbed CO_2 was observed (Table 4). Similarly, Ni/Y_2O_3 catalysts exhibited predominantly weak and moderate basic sites (Figure 8b) [36,38,95]. In particular, the amount of basic sites increased with Ni loading, with the exception of the $7Ni/Y_2O_3$ system (Table 4). Indeed, the following basicity order was determined: $15Ni/Y_2O_3$ (104.04 $\mu mol_{CO2}\cdot g^{-1}$) < $25Ni/Y_2O_3$ (130.66 $\mu mol_{CO2}\cdot g^{-1}$) < $7Ni/Y_2O_3$ (154.44 $\mu mol_{CO2}\cdot g^{-1}$) < $35Ni/Y_2O_3$ (188.46 $\mu mol_{CO2}\cdot g^{-1}$). This indicated that the Ni phase acted as basic site for CO_2 adsorption, while the relatively high surface area of $7Ni/Y_2O_3$ (40.7 $m^2\cdot g^{-1}$) should be the reason for the large amount of desorbed CO_2 [33]. Therefore, the basic site density, expressed as CO_2 desorbed per unit surface area of catalyst, increased with the nickel content (Table 4).

3.2. CO and CO_2 methanation activity tests

The comparison of the catalytic performances of the Ni-based catalysts supported on CeO_2, Al_2O_3 and Y_2O_3 oxides can be found in Figure 9. Not stable activity was evidenced for the $15Ni/CeO_2$ catalyst (Fugure 9a), for which both CO and CO_2 conversions decreased with time after 2 h at 300°C. Otherwise, $15Ni/Al_2O_3$ (Figure 9b) and $15Ni/Y_2O_3$ (Figure 9c) showed a volcano-shaped trend with the increase of reaction temperature. Since both CO and CO_2 hydrogenation reactions are strongly exothermic, low temperature was thermodynamically beneficial but kinetically disadvantage to the reaction due to the slow reaction rate [10,52,97]. Indeed, 350 and 350°C were needed to achieve the total CO conversion over the Al_2O_3- and Y_2O_3-supported catalysts, respectively. Besides, CO_2 conversion increased with temperature and then reached a maximal value at ca. 350-400°C. The CO_2 conversion over $15Ni/Y_2O_3$ was 71.5% at 350°C, higher than the maximum value over $15Ni/Al_2O_3$ (57.4%) at 400°C, pointing out the high activity of the former catalyst towards the methanation reaction. Then, a further increase in the reaction temperature led to a slight decrease in both CO and CO_2 conversions, in agreement with the thermodynamic calculations (not shown) [98,99].

Figure 10 shows the catalytic activity of the Ni/Y_2O_3 catalysts with different Ni loading (7-35 wt.%). The dashed lines corresponded to the equilibrium values from the thermodynamic calculations. It is likely that CO interact more strongly with metal surface than CO_2 [68,100]. Thus, the complete removal of CO was observed at 300°C for all the studied systems (Figure 10a). Furthermore, with increased metal loading, CO_2 conversion increased and a lower conversion temperature was achieved. As an example, the CO_2 conversion at 300°C increased as follows: $7Ni/Y_2O_3$ (35.8%) < $15Ni/Y_2O_3$ (53.3%) < $25Ni/Y_2O_3$ (69.8%) (Figure 10b). However, at high metal loading (35 wt.%), the CO_2 conversion (75.4) did not significantly increased, probably due to the formation of enlarged metal particles (Table 1). Similarly, CH_4 yield increased with temperature, indicating a kinetically-controlled reaction at relatively low temperature; then it reached a maximum value at ca. 350°C, decreasing afterward due to thermodynamic limit of methanation reactions and to the occurrence of RWGS reaction [22,52]. In addition, among the studied catalysts, the $35Ni/Y_2O_3$ showed the best performance, leading to the total CO conversion as well as the highest CO_2 conversion (83.5%) and CH_4 yield (90.3%) at 350°C.

3.3. Correlations between physico-chemical properties and catalytic performance

As discussed by Yan et al. [38], a fine-tuning of the Ni-support interactions is strictly necessary to obtain active and stable catalysts for CO and CO_2 methanation. In particular, too weak metal-support interaction led to sintering of Ni particles due to the high mobility of the $Ni(CO)_4$ species [51]. Whereas, too strong Ni-support interaction decreased the number of exposed Ni sites, being them chemically linked to the matrix of the support [101,102]. Moreover, also the nature and distribution of surface basic sites for CO_2 adsorption played a key role in achieving high methanation performances [52,98].

In this study, Ni-support interactions clearly dependent on the type of oxide support were evidenced from H_2-TPR profiles, following the order $Ni/CeO_2 < Ni/Y_2O_3 < Ni/Al_2O_3$ (Figure 4a). The relatively weak metal-support interaction of the $15Ni/CeO_2$ catalyst (Figure x) resulted in catalytic performance degradation that could depend on the vulnerability to CO-poisoning of Ni active sites [16,103]. Moreover, the valence change between Ce^{3+} and Ce^{4+} facilitated the direct dissociated adsorption of CO, resulting in the deposition of carbon as evinced from TEM characterization of the used catalysts, showing both encapsulating and filamentous carbon species (Figures 11a,b,c) [10]. Otherwise, high anti-coking ability was observed for both $15Ni/Al_2O_3$ (Figure 11d) and $15Ni/Y_2O_3$ catalysts (Figure 11e). However, the formation of $NiAl_2O_4$ spinel, regarded as non-active species in methanation reaction, was the main reason of the lower activity of the Al_2O_3-supported system compared to the Y_2O_3-supported catalyst [104]. Similar results were previously reported by Cui et al. [59]. The Authors found that a too strong metal-support interaction lowered the ratio of NiO species to nickel aluminates, negatively affecting the activity and stability of Ni/Al_2O_3 catalyst towards syngas methanation [59].

In between, the moderate Ni-Y_2O_3 interactions explained the superior performance of the $15Ni/Y_2O_3$ catalyst, while the beneficial effect of Ni content was strongly connected to the basic properties of the catalyst [52]. Indeed, although the reaction pathways and mechanisms of the hydrogenation of CO_2 to CH_4 is still under debate, it is accepted that CO_2 adsorbed over the basic sites [52,98,102,105]. It is observed that, under the experimental conditions employed, the higher the nickel content, the higher the CO_2 conversion was in almost the entire temperature range (Figure 10). The intrinsic CO_2 methanation rates per unit mass of nickel per second were calculated at 300°C. The CO_2 conversion rates decreased by increasing the Ni crystal size, as follows: $7Ni/Y_2O_3$ ($1.13x10^{-4}$ $mol \cdot s^{-1} \cdot gNi^{-1}$) > $15Ni/Y_2O_3$ ($8.05x10^{-5}$ $mol \cdot s^{-1} \cdot gNi^{-1}$) > $25Ni/Y_2O_3$ ($6.31x10^{-5}$ $mol \cdot s^{-1} \cdot gNi^{-1}$) > $35Ni/Y_2O_3$ ($4.91x10^{-5}$ $mol \cdot s^{-1} \cdot gNi^{-1}$). These results indicated that the CO_2 methanation at relatively low temperature (300°C) over Ni/Y_2O_3 catalysts was a structure-sensitive reaction, as previously reported by other authors [106,107]. It could be concluded that the CO_2 hydrogenation on Ni/Y_2O_3 increased with decreasing mean Ni crystallite size. Indeed, as the nickel content increased, the exposed surface area decreased leading to lower methanation rate, while smaller Ni particles were significantly more efficient in catalyzing CO_2 hydrogenation.

In addition, the turnover frequency of CO_2 conversion over the Y_2O_3-supported samples with variable metal loading were calculated and compared with CO_2-TPD results. The results shown in Figure 12 suggested that the CO_2 hydrogenation to CH_4 was greatly affected by the nature of active centers rather than the number of active centers available to perform methanation reaction [108]. In particular, it should be noted that the activity sequence followed the order of the medium basicity. Indeed, the moderate basic sites would be one of the desired properties of Ni catalyst for the SNG production from CO_2 methanation, as previously reported by Muroyama et al. [33].

3.4. CO and CO_2 methanation stability test

Figure 13 shows the lifetime test results of the 25Ni/Y_2O_3 catalyst, tested at atmospheric pressure, reaction temperature of 350°C and GHSV of 10,000 h^{-1}. Stable CO conversion was observed aver 200 h of time-on-stream, while CO_2 conversion and CH_4 yield decreased slightly but still quite stable. Moreover, the Ni particle size did not significantly increased for the spent catalyst, as shown in Figure 11f, also evidencing no obvious evidence of deposited C-species.

4. Conclusions

The CO and CO_2 methanation was studied over Ni-based catalysts supported on CeO_2, Al_2O_3, and Y_2O_3 oxides. Results show that the catalytic activity strongly depended on the nature of the Ni-oxide interactions. Ni/CeO_2 catalyst deactivated quickly due to coke accumulation as a consequence of the CO-poisoning of weakly-interacted Ni active sites. In contrast, the formation of $NiAl_2O_4$ spinel lowered the quantity of active Ni species decreasing, in turn, the catalytic activity of the Ni/Al_2O_3 catalyst.

The moderate Ni-support interactions explained the superior performance of the Y_2O_3-supported catalysts, for which the higher the nickel content, the higher the activity mainly in term of CO_2 conversion and CH_4 yield. A volcano-shaped trend with the increase of reaction temperature was observed, indicating a kinetically-controlled reaction at relatively low temperature as well as a thermodynamic-controlled reaction at higher temperature. CO_2 methanation rates per unit mass of nickel decreased with the Ni content (or Ni crystal size) accounting for a structure-sensitive reaction. Moreover, the best correlation between basic surface properties and activity data suggested that moderate-basic sites had a positive effect on the catalytic activity for CO and CO_2 hydrogenation. Finally, good anti-coking and anti-sintering ability after 200 h of lifetime test make 25Ni/Y_2O_3 an effective catalyst for the production of SNG.

Acknowledgments

This work was funded by the Italian Ministry of Economic Development in the framework of the “Fondo per la Ricerca di Sistema Elettrico - Piano Triennale 2015-2017 - Progetto Sistemi Elettrochimici per l’accumulo di energia”. JL is a Serra Húnter Fellow and is grateful to ICREA Academia program and GC 2017 SGR 128.

References

[1] F. Gutiérrez-Martín, L.M. Rodríguez-Antón, Power-to-SNG technologies by hydrogenation of CO2 and biomass resources: A comparative chemical engineering process analysis, Int. J. Hydrogen Energy. (2018). doi:https://doi.org/10.1016/j.ijhydene.2018.09.168.

[2] R. Anghilante, C. Müller, M. Schmid, D. Colomar, F. Ortloff, R. Spörl, A. Brisse, F. Graf, Innovative power-to-gas plant concepts for upgrading of gasification bio-syngas through steam electrolysis and catalytic methanation, 183 (2019) 462–473.

[3] M. Sarić, J.W. Dijkstra, W.G. Haije, Economic perspectives of Power-to-Gas technologies in bio-methane production, J. CO2 Util. 20 (2017) 81–90. doi:10.1016/j.jcou.2017.05.007.

[4] P. Sabatier, J.B. Senderens, New synthesis of methane, Compt. Rend. 134 (1902) 514–516.

[5] A. Zhao, W. Ying, H. Zhang, M. Hongfang, D. Fang, Ni/Al 2O 3 catalysts for syngas methanation: Effect of Mn promoter, J. Nat. Gas Chem. 21 (2012) 170–177. doi:10.1016/S1003-9953(11)60350-2.

[6] M. Tao, X. Meng, Z. Xin, Z. Bian, Y. Lv, J. Gu, Synthesis and characterization of well dispersed nickel-incorporated SBA-15 and its high activity in syngas methanation reaction, Appl. Catal. A Gen. 516 (2016) 127–134. doi:10.1016/j.apcata.2016.02.019.

[7] I. Kuznecova, J. Gusca, ScienceDirect ScienceDirect Property based ranking of CO and CO2 methanation catalysts, Energy Procedia. 128 (2017) 255–260. doi:10.1016/j.egypro.2017.09.068.

[8] X. Lu, F. Gu, Q. Liu, J. Gao, Y. Liu, H. Li, L. Jia, G. Xu, Z. Zhong, F. Su, VOx promoted Ni catalysts supported on the modified bentonite for CO and CO2 methanation, Fuel Process. Technol. 135 (2015) 34–46. doi:10.1016/j.fuproc.2014.10.009.

[9] M.-Y. Ding, J.-Y. Tu, T.-J. Wang, L.-L. Ma, C.-G. Wang, L.-G. Chen, Bio-syngas methanation towards synthetic natural gas (SNG) over highly active Al2O3-CeO2 supported Ni catalyst, Fuel Process. Technol. 134 (2015) 480–486. doi:10.1016/j.fuproc.2015.03.006.

[10] H. Lu, X. Yang, G. Gao, J. Wang, C. Han, X. Liang, C. Li, Y. Li, W. Zhang, X. Chen, Metal (Fe , Co , Ce or La) doped nickel catalyst supported on ZrO 2 modified mesoporous clays for CO and CO 2 methanation, 183 (2016) 335–344.

[11] W.H. Chen, M.R. Lin, T.S. Leu, S.W. Du, An evaluation of hydrogen production from the perspective of using blast furnace gas and coke oven gas as feedstocks, Int. J. Hydrogen Energy. 36 (2011) 11727–11737. doi:10.1016/j.ijhydene.2011.06.049.

[12] W. Li, C. Wang, H. Wang, J. Chen, C. Yuan, T. Li, W. Wang, H. Shen, Y. Huang, R. Wang, B. Wang, Y. Zhang, H. Chen, Y. Chen, J. Tang, X. Wang, J. Liu, R.M. Coveney, S. Tao, Distribution of atmospheric particulate matter (PM) in rural field, rural village and urban areas of northern China, Environ. Pollut. 185 (2014) 134–140. doi:10.1016/j.envpol.2013.10.042.

[13] T.A. Le, M.S. Kim, S.H. Lee, T.W. Kim, E.D. Park, CO and CO2 methanation over supported Ni catalysts, Catal. Today. 293–294 (2017) 89–96. doi:10.1016/j.cattod.2016.12.036.

[14] B. Zhao, Z. Chen, Y. Chen, X. Ma, Syngas methanation over Ni/SiO2 catalyst prepared by ammonia-assisted impregnation, Int. J. Hydrogen Energy. 42 (2017) 27073–27083. doi:10.1016/j.ijhydene.2017.09.068.

[15] X. Su, J. Xu, B. Liang, H. Duan, B. Hou, Y. Huang, Catalytic carbon dioxide hydrogenation to methane: A review of recent studies, J. Energy Chem. 25 (2016) 553–565. doi:https://doi.org/10.1016/j.jechem.2016.03.009.

[16] J.R. Rostrup-Nielsen, K. Pedersen, J. Sehested, High temperature methanation. Sintering and structure sensitivity, Appl. Catal. A Gen. 330 (2007) 134–138. doi:10.1016/j.apcata.2007.07.015.

[17] S. Ratchahat, Y. Suzuki, R. Watanabe, C. Fukuhara, W. Kawasaki, M. Sudoh, Development of a powerful CO 2 methanation process using a structured Ni/CeO 2 catalyst, J. CO2 Util. 24 (2018) 210–219. doi:10.1016/j.jcou.2018.01.004.

[18] P. Panagiotopoulou, D.I. Kondarides, X.E. Verykios, Selective methanation of CO over supported noble metal

catalysts: Effects of the nature of the metallic phase on catalytic performance, Appl. Catal. A Gen. 344 (2008) 45–54. doi:https://doi.org/10.1016/j.apcata.2008.03.039.

[19] K. Jalama, Carbon dioxide hydrogenation over nickel-, ruthenium-, and copper-based catalysts: Review of kinetics and mechanism, Catal. Rev. - Sci. Eng. 59 (2017) 95–164. doi:10.1080/01614940.2017.1316172.

[20] A.L. Kustov, A.M. Frey, K.E. Larsen, T. Johannessen, J.K. Nørskov, C.H. Christensen, CO methanation over supported bimetallic Ni–Fe catalysts: From computational studies towards catalyst optimization, Appl. Catal. A Gen. 320 (2007) 98–104. doi:https://doi.org/10.1016/j.apcata.2006.12.017.

[21] S. Tada, S. Ikeda, N. Shimoda, T. Honma, M. Takahashi, A. Nariyuki, S. Satokawa, Sponge Ni catalyst with high activity in CO2 methanation, Int. J. Hydrogen Energy. 42 (2017) 30126–30134. doi:https://doi.org/10.1016/j.ijhydene.2017.10.138.

[22] K. Stangeland, D.Y. Kalai, H. Li, Z. Yu, Active and stable Ni based catalysts and processes for biogas upgrading: The effect of temperature and initial methane concentration on CO2 methanation, Appl. Energy. 227 (2018) 206–212. doi:https://doi.org/10.1016/j.apenergy.2017.08.080.

[23] F. Feng, G. Song, J. Xiao, L. Shen, S. V. Pisupati, Carbon deposition on Ni-based catalyst with TiO2 as additive during the syngas methanation process in a fluidized bed reactor, Fuel. 235 (2019) 85–91. doi:10.1016/j.fuel.2018.07.076.

[24] R. Razzaq, H. Zhu, L. Jiang, U. Muhammad, C. Li, S. Zhang, Catalytic methanation of CO and CO2 in coke oven gas over Ni-Co/ZrO2-CeO2, Ind. Eng. Chem. Res. 52 (2013) 2247–2256. doi:10.1021/ie301399z.

[25] A. Kokka, T. Ramantani, A. Petala, P. Panagiotopoulou, Effect of the nature of the support, operating and pretreatment conditions on the catalytic performance of supported Ni catalysts for the selective methanation of CO, Catal. Today. (2019). doi:https://doi.org/10.1016/j.cattod.2019.04.015.

[26] T.A. Le, T.W. Kim, S.H. Lee, E.D. Park, Effects of Na content in Na/Ni/SiO2 and Na/Ni/CeO2 catalysts for CO and CO2 methanation, Catal. Today. 303 (2018) 159–167. doi:https://doi.org/10.1016/j.cattod.2017.09.031.

[27] R. Zhou, N. Rui, Z. Fan, C. Liu, Effect of the structure of Ni/TiO2 catalyst on CO2 methanation, Int. J. Hydrogen Energy. 41 (2016) 22017–22025. doi:https://doi.org/10.1016/j.ijhydene.2016.08.093.

[28] X. Jia, X. Zhang, N. Rui, X. Hu, C. Liu, Structural effect of Ni/ZrO2 catalyst on CO2 methanation with enhanced activity, Appl. Catal. B Environ. 244 (2019) 159–169. doi:https://doi.org/10.1016/j.apcatb.2018.11.024.

[29] D.C.D. da Silva, S. Letichevsky, L.E.P. Borges, L.G. Appel, The Ni/ZrO2 catalyst and the methanation of CO and CO2, Int. J. Hydrogen Energy. 37 (2012) 8923–8928. doi:https://doi.org/10.1016/j.ijhydene.2012.03.020.

[30] Z. Bian, Y.M. Chan, Y. Yu, S. Kawi, Morphology dependence of catalytic properties of Ni/CeO2 for CO2 methanation: A kinetic and mechanism study, Catal. Today. (2018). doi:https://doi.org/10.1016/j.cattod.2018.04.067.

[31] F. Meng, Z. Li, F. Ji, M. Li, Effect of ZrO2 on catalyst structure and catalytic methanation performance over Ni-based catalyst in slurry-bed reactor, Int. J. Hydrogen Energy. 40 (2015) 8833–8843. doi:https://doi.org/10.1016/j.ijhydene.2015.05.057.

[32] S.I. Fujita, N. Takezawa, Difference in the selectivity of CO and CO2 methanation reactions, Chem. Eng. J. 68 (1997) 63–68. doi:10.1016/S1385-8947(97)00074-0.

[33] H. Muroyama, Y. Tsuda, T. Asakoshi, H. Masitah, T. Okanishi, T. Matsui, K. Eguchi, Carbon dioxide methanation over Ni catalysts supported on various metal oxides, J. Catal. 343 (2016) 178–184. doi:https://doi.org/10.1016/j.jcat.2016.07.018.

[34] Y. Wang, K. Zheng, X. Hu, W. Zhou, X. Wei, Y. Zhao, Y2O3 promoted Co3O4 catalyst for catalytic decomposition of N2O, Mol. Catal. 470 (2019) 104–111. doi:https://doi.org/10.1016/j.mcat.2019.04.002.

[35] J.D.A. Bellido, E.M. Assaf, Effect of the Y2O3–ZrO2 support composition on nickel catalyst evaluated in dry reforming of methane, Appl. Catal. A Gen. 352 (2009) 179–187. doi:https://doi.org/10.1016/j.apcata.2008.10.002.

[36] H. Liu, H. Wu, D. He, Methane conversion to syngas over Ni/Y2O3 catalysts — Effects of calcination temperatures of Y2O3 on physicochemical properties and catalytic performance, Fuel Process. Technol. 119 (2014) 81–86. doi:https://doi.org/10.1016/j.fuproc.2013.11.001.

[37] M. Lo Faro, S. Trocino, S.C. Zignani, A.S. Aricò, G. Maggio, C. Italiano, C. Fabiano, L. Pino, A. Vita, Study of a Solid Oxide Fuel Cell fed with n-dodecane reformate. Part I: Endurance test, Int. J. Hydrogen Energy. 41 (2016) 5741–5747. doi:https://doi.org/10.1016/j.ijhydene.2016.02.119.

[38] Y. Yan, Y. Dai, Y. Yang, A.A. Lapkin, Improved stability of Y2O3 supported Ni catalysts for CO2 methanation by precursor-determined metal-support interaction, Appl. Catal. B Environ. 237 (2018) 504–512. doi:https://doi.org/10.1016/j.apcatb.2018.06.021.

[39] C. Italiano, A. Vita, C. Fabiano, M. Laganà, L. Pino, Bio-hydrogen production by oxidative steam reforming of biogas over nanocrystalline Ni/CeO2 catalysts, Int. J. Hydrogen Energy. 40 (2015) 11823–11830. doi:10.1016/j.ijhydene.2015.04.146.

[40] A. Vita, C. Italiano, C. Fabiano, M. Laganà, L. Pino, Influence of Ce-precursor and fuel on structure and catalytic activity of combustion synthesized Ni/CeO<inf>2</inf> catalysts for biogas oxidative steam reforming, Mater. Chem. Phys. 163 (2015) 337–347. doi:10.1016/j.matchemphys.2015.07.048.

[41] K. Ray, G. Deo, A potential descriptor for the CO2 hydrogenation to CH4 over Al2O3 supported Ni and Ni-based alloy catalysts, Appl. Catal. B Environ. 218 (2017) 525–537. doi:https://doi.org/10.1016/j.apcatb.2017.07.009.

[42] O. Al, J. Lin, C. Ma, Q. Wang, Y. Xu, G. Ma, J. Wang, Applied Catalysis B : Environmental Enhanced low-temperature performance of CO 2 methanation over, Appl. Catal. B Environ. 243 (2019) 262–272. doi:10.1016/j.apcatb.2018.10.059.

[43] N.D. Charisiou, M.A. Baker, K. Polychronopoulou, V. Sebastian, L. Tzounis, S.J. Hinder, M.A. Goula, Investigating the correlation between deactivation and the carbon deposited on the surface of Ni/Al 2 O 3 and Ni/La 2 O 3 -Al 2 O 3 catalysts during the biogas reforming reaction, Appl. Surf. Sci. 474 (2018) 42–56. doi:10.1016/j.apsusc.2018.05.177.

[44] F.J. Sotomayor, K.A. Cychosz, M. Thommes, Characterization of Micro/Mesoporous Materials by Physisorption : Concepts and Case Studies, Acc. Mater. Surf. Res. 3 (2018) 36–37. https://www.hyomen.org/wp-content/uploads/papers/vol3_no2/sotomayor/sotomayor_40.pdf.

[45] A. Muñoz-Murillo, L.M. Martínez T., M.I. Domínguez, J.A. Odriozola, M.A. Centeno, Selective CO methanation with structured RuO2/Al2O3 catalysts, Appl. Catal. B Environ. 236 (2018) 420–427. doi:https://doi.org/10.1016/j.apcatb.2018.05.020.

[46] H. Zhang, H. Lu, Y. Zhu, F. Li, R. Duan, M. Zhang, X. Wang, Preparations and characterizations of new mesoporous ZrO 2 and Y 2O 3-stabilized ZrO 2 spherical powders, Powder Technol. 227 (2012) 9–16. doi:10.1016/j.powtec.2012.02.007.

[47] Y. XU, X. DU, J. LI, P. WANG, J. ZHU, F. GE, J. ZHOU, M. SONG, W. ZHU, A comparison of Al2O3 and SiO2 supported Ni-based catalysts in their performance for the dry reforming of methane, J. Fuel Chem. Technol. 47 (2019) 199–208. doi:10.1016/s1872-5813(19)30010-6.

[48] A. Alhaji, R.S. Razavi, A. Ghasemi, crossmark, 43 (2017) 2541–2548.

[49] Y.T. Foo, A.Z. Abdullah, B.A. Horri, B. Salamatinia, Synthesis and characterisation of Y2O3 using ammonia oxalate as a precipitant in distillate pack co-precipitation process, Ceram. Int. 44 (2018) 18693–18702. doi:https://doi.org/10.1016/j.ceramint.2018.07.098.

[50] L. Yang, C. Peng, X. Fang, Z. Cheng, Z. Zhou, Hierarchically macro-mesoporous Ni-Mo/Al2O3 catalysts for hydrodesulfurization of dibenzothiophene, Catal. Commun. 121 (2019) 68–72. doi:https://doi.org/10.1016/j.catcom.2018.12.020.

[51] B. Nematollahi, M. Rezaei, E.N. Lay, Preparation of highly active and stable NiO–CeO2 nanocatalysts for CO selective methanation, Int. J. Hydrogen Energy. 40 (2015) 8539–8547. doi:https://doi.org/10.1016/j.ijhydene.2015.04.127.

[52] A. Vita, C. Italiano, L. Pino, P. Frontera, M. Ferraro, V. Antonucci, Activity and stability of powder and

monolith-coated Ni/GDC catalysts for CO2 methanation, Appl. Catal. B Environ. 226 (2018) 384–395. doi:10.1016/j.apcatb.2017.12.078.

[53] S. Chen, G. Zhou, H. Xie, Z. Jiao, X. Zhang, Hydrodeoxygenation of methyl laurate over the sulfur-free Ni/γ-Al2O3 catalysts, Appl. Catal. A Gen. 569 (2019) 35–44. doi:https://doi.org/10.1016/j.apcata.2018.10.014.

[54] V. V. Galvita, H. Poelman, V. Bliznuk, C. Detavernier, G.B. Marin, CeO_2 -Modified Fe_2O_3 for CO_2 Utilization via Chemical Looping, Ind. Eng. Chem. Res. 52 (2013) 8416–8426. doi:10.1021/ie4003574.

[55] B. Mandal, A. Mondal, S.S. Ray, A. Kundu, Sm doped mesoporous CeO2nanocrystals: Aqueous solution-based surfactant assisted low temperature synthesis, characterization and their improved autocatalytic activity, Dalt. Trans. 45 (2016) 1679–1692. doi:10.1039/c5dt03688g.

[56] C. Italiano, N.T.J. Luchters, L. Pino, J. V. Fletcher, S. Specchia, J.C.Q. Fletcher, A. Vita, High specific surface area supports for highly active Rh catalysts: Syngas production from methane at high space velocity, Int. J. Hydrogen Energy. 43 (2018) 11755–11765. doi:10.1016/j.ijhydene.2018.01.136.

[57] R. Dey, V.K. Rai, pH controlled Ho3+–Yb3+ codoped Y2O3 nanowires for display devices, Spectrochim. Acta Part A Mol. Biomol. Spectrosc. 151 (2015) 213–217. doi:https://doi.org/10.1016/j.saa.2015.06.047.

[58] Y. Liu, M.L. Qin, L. Zhang, B.R. Jia, Z.Q. Cao, D.Z. Zhang, X.H. Qu, Solution combustion synthesis of Ni-Y2O3 nanocomposite powder, Trans. Nonferrous Met. Soc. China (English Ed. 25 (2015) 129–136. doi:10.1016/S1003-6326(15)63587-7.

[59] D. Cui, J. Liu, J. Yu, J. Yue, F. Su, G. Xu, Necessity of moderate metal-support interaction in Ni/Al2O3 for syngas methanation at high temperatures, RSC Adv. 5 (2015) 10187–10196. doi:10.1039/c4ra14652b.

[60] Z. Fang, D. Shi, N. Lin, A. Li, Q. Wu, Q. Wang, Y. Zhao, C. Feng, Q. Jiao, H. Li, Probing the synergistic effect of Mo on Ni-based catalyst in the hydrogenation of dicyclopentadiene, Appl. Catal. A Gen. 574 (2019) 60–70. doi:https://doi.org/10.1016/j.apcata.2019.01.026.

[61] M.H. Youn, J.G. Seo, P. Kim, I.K. Song, Role and effect of molybdenum on the performance of Ni-Mo/γ-Al2O3 catalysts in the hydrogen production by auto-thermal reforming of ethanol, J. Mol. Catal. A Chem. 261 (2007) 276–281. doi:https://doi.org/10.1016/j.molcata.2006.08.030.

[62] X. Zou, X. Wang, L. Li, K. Shen, X. Lu, W. Ding, Development of highly effective supported nickel catalysts for pre-reforming of liquefied petroleum gas under low steam to carbon molar ratios, Int. J. Hydrogen Energy. 35 (2010) 12191–12200. doi:https://doi.org/10.1016/j.ijhydene.2010.08.080.

[63] C. Italiano, R. Balzarotti, A. Vita, S. Latorrata, C. Fabiano, L. Pino, C. Cristiani, Preparation of structured catalysts with Ni and Ni–Rh/CeO2 catalytic layers for syngas production by biogas reforming processes, Catal. Today. 273 (2016) 3–11. doi:10.1016/j.cattod.2016.01.037.

[64] T. V Sagar, N. Sreelatha, G. Hanmant, M. Surendar, N. Lingaiah, K.S. Rama Rao, C.V. V Satyanarayana, I.A.K. Reddy, P.S. Sai Prasad, Influence of method of preparation on the activity of La–Ni–Ce mixed oxide catalysts for dry reforming of methane, RSC Adv. 4 (2014) 50226–50232. doi:10.1039/C4RA07098D.

[65] R.K. Singha, A. Shukla, A. Yadav, L.N. Sivakumar Konathala, R. Bal, Effect of metal-support interaction on activity and stability of Ni-CeO2 catalyst for partial oxidation of methane, Appl. Catal. B Environ. 202 (2017) 473–488. doi:https://doi.org/10.1016/j.apcatb.2016.09.060.

[66] H. Liu, D. He, Properties of Ni/Y2O3 and its catalytic performance in methane conversion to syngas, Int. J. Hydrogen Energy. 36 (2011) 14447–14454. doi:https://doi.org/10.1016/j.ijhydene.2011.08.025.

[67] V.G. Deshmane, S.L. Owen, R.Y. Abrokwah, D. Kuila, Mesoporous nanocrystalline TiO2 supported metal (Cu, Co, Ni, Pd, Zn, and Sn) catalysts: Effect of metal-support interactions on steam reforming of methanol, J. Mol. Catal. A Chem. 408 (2015) 202–213. doi:https://doi.org/10.1016/j.molcata.2015.07.023.

[68] R. Daroughegi, F. Meshkani, M. Rezaei, Enhanced activity of CO2 methanation over mesoporous nanocrystalline Ni–Al2O3 catalysts prepared by ultrasound-assisted co-precipitation method, Int. J. Hydrogen Energy. 42 (2017) 15115–15125. doi:https://doi.org/10.1016/j.ijhydene.2017.04.244.

[69] W. Nie, X. Zou, X. Shang, X. Wang, W. Ding, X. Lu, CeO2-assisted Ni nanocatalysts supported on mesoporous γ-Al2O3 for the production of synthetic natural gas, Fuel. 202 (2017) 135–143.

doi:https://doi.org/10.1016/j.fuel.2017.04.026.

[70] R.K. Singha, A. Yadav, A. Agrawal, A. Shukla, S. Adak, T. Sasaki, R. Bal, Synthesis of highly coke resistant Ni nanoparticles supported MgO/ZnO catalyst for reforming of methane with carbon dioxide, Appl. Catal. B Environ. 191 (2016) 165–178. doi:https://doi.org/10.1016/j.apcatb.2016.03.029.

[71] W.-P. Dow, Y.-P. Wang, T.-J. Huang, Yttria-Stabilized Zirconia Supported Copper Oxide Catalyst: I. Effect of Oxygen Vacancy of Support on Copper Oxide Reduction, J. Catal. 160 (1996) 155–170. doi:https://doi.org/10.1006/jcat.1996.0135.

[72] M. Zabilskiy, P. Djinović, E. Tchernychova, O.P. Tkachenko, L.M. Kustov, A. Pintar, Nanoshaped CuO/CeO2 Materials: Effect of the Exposed Ceria Surfaces on Catalytic Activity in N2O Decomposition Reaction, ACS Catal. 5 (2015) 5357–5365. doi:10.1021/acscatal.5b01044.

[73] A. Boukerika, L. Guerbous, Annealing effects on structural and luminescence properties of red Eu3+-doped Y2O3 nanophosphors prepared by sol–gel method, J. Lumin. 145 (2014) 148–153. doi:https://doi.org/10.1016/j.jlumin.2013.07.037.

[74] Y. Wang, L. Wang, N. Gan, Z.-Y. Lim, C. Wu, J. Peng, W.G. Wang, Evaluation of Ni/Y2O3/Al2O3 catalysts for hydrogen production by autothermal reforming of methane, Int. J. Hydrogen Energy. 39 (2014) 10971–10979. doi:https://doi.org/10.1016/j.ijhydene.2014.05.074.

[75] P. Kim, Y. Kim, C. Kim, H. Kim, Y. Park, J.H. Lee, I.K. Song, J. Yi, Synthesis and Characterization of Mesoporous Alumina as a Catalyst Support for Hydrodechlorination of 1,2-Dichloropropane: Effect of Catalyst Preparation Method, Catal. Letters. 89 (2003) 185–192. doi:10.1023/A:1025794127243.

[76] L. Pino, C. Italiano, A. Vita, M. Laganà, V. Recupero, Ce0.70La0.20Ni0.10O2-Δ catalyst for methane dry reforming: Influence of reduction temperature on the catalytic activity and stability, Appl. Catal. B Environ. 218 (2017) 779–792. doi:10.1016/j.apcatb.2017.06.080.

[77] M.Á. Centeno, C. Portales, I. Carrizosa, J.A. Odriozola, Gold supported CeO2/Al2O3 catalysts for CO oxidation: influence of the ceria phase, Catal. Letters. 102 (2005) 289–297. doi:10.1007/s10562-005-5871-5.

[78] H. Razavi-Khosroshahi, K. Edalati, H. Emami, E. Akiba, Z. Horita, M. Fuji, Optical Properties of Nanocrystalline Monoclinic Y2O3 Stabilized by Grain Size and Plastic Strain Effects via High-Pressure Torsion, Inorg. Chem. 56 (2017) 2576–2580. doi:10.1021/acs.inorgchem.6b02725.

[79] B.N. Lakshminarasappa, J.R. Jayaramaiah, B.M. Nagabhushana, Thermoluminescence of combustion synthesized yttrium oxide, Powder Technol. 217 (2012) 7–10. doi:https://doi.org/10.1016/j.powtec.2011.09.042.

[80] I. Tanaka, F. Oba, K. Tatsumi, M. Kunisu, M. Nakano, H. Adachi, Theoretical Formation Energy of Oxygen-Vacancies in Oxides, Mater. Trans. 43 (2002) 1426–1429. doi:10.2320/matertrans.43.1426.

[81] R.H. Krishna, B.M. Nagabhushana, H. Nagabhushana, N.S. Murthy, S.C. Sharma, C. Shivakumara, R.P.S. Chakradhar, Effect of Calcination Temperature on Structural, Photoluminescence, and Thermoluminescence Properties of Y2O3:Eu3+ Nanophosphor, J. Phys. Chem. C. 117 (2013) 1915–1924. doi:10.1021/jp309684b.

[82] Y. Kumar, M. Pal, M. Herrera, X. Mathew, Effect of Eu ion incorporation on the emission behavior of Y2O3 nanophosphors: A detailed study of structural and optical properties, Opt. Mater. (Amst). 60 (2016) 159–168. doi:https://doi.org/10.1016/j.optmat.2016.07.026.

[83] M.C. Bacariza, I. Graça, S.S. Bebiano, J.M. Lopes, C. Henriques, Micro- and mesoporous supports for CO2 methanation catalysts: A comparison between SBA-15, MCM-41 and USY zeolite, Chem. Eng. Sci. 175 (2018) 72–83. doi:https://doi.org/10.1016/j.ces.2017.09.027.

[84] X. Ning, Y. Lu, H. Fu, H. Wan, Z. Xu, S. Zheng, Template-Mediated Ni(II) Dispersion in Mesoporous SiO2 for Preparation of Highly Dispersed Ni Catalysts: Influence of Template Type, ACS Appl. Mater. Interfaces. 9 (2017) 19335–19344. doi:10.1021/acsami.7b04100.

[85] S. Ewald, M. Kolbeck, T. Kratky, M. Wolf, O. Hinrichsen, On the deactivation of Ni-Al catalysts in CO2 methanation, Appl. Catal. A Gen. 570 (2019) 376–386. doi:https://doi.org/10.1016/j.apcata.2018.10.033.

[86] E. Kordouli, B. Pawelec, C. Kordulis, A. Lycourghiotis, J.L.G. Fierro, Hydrodeoxygenation of phenol on

bifunctional Ni-based catalysts: Effects of Mo promotion and support, Appl. Catal. B Environ. 238 (2018) 147–160. doi:https://doi.org/10.1016/j.apcatb.2018.07.012.

[87] J. Du, J. Gao, F. Gu, J. Zhuang, B. Lu, L. Jia, G. Xu, Q. Liu, F. Su, A strategy to regenerate coked and sintered Ni/Al2O3 catalyst for methanation reaction, Int. J. Hydrogen Energy. 43 (2018) 20661–20670. doi:https://doi.org/10.1016/j.ijhydene.2018.09.128.

[88] G. Zhou, H. Liu, K. Cui, A. Jia, G. Hu, Z. Jiao, Y. Liu, X. Zhang, Role of surface Ni and Ce species of Ni/CeO2 catalyst in CO2 methanation, Appl. Surf. Sci. 383 (2016) 248–252. doi:https://doi.org/10.1016/j.apsusc.2016.04.180.

[89] M. Li, A.C. van Veen, Tuning the catalytic performance of Ni-catalysed dry reforming of methane and carbon deposition via Ni-CeO2-x interaction, Appl. Catal. B Environ. 237 (2018) 641–648. doi:https://doi.org/10.1016/j.apcatb.2018.06.032.

[90] A. Quindimil, U. De-La-Torre, B. Pereda-Ayo, J.A. González-Marcos, J.R. González-Velasco, Ni catalysts with La as promoter supported over Y- and BETA- zeolites for CO2 methanation, Appl. Catal. B Environ. 238 (2018) 393–403. doi:https://doi.org/10.1016/j.apcatb.2018.07.034.

[91] I. Pettiti, D. Gazzoli, P. Benito, G. Fornasari, A. Vaccari, The reducibility of highly stable Ni-containing species in catalysts derived from hydrotalcite-type precursors, RSC Adv. 5 (2015) 82282–82291. doi:10.1039/C5RA13863A.

[92] J.M. Sanz, G.T. Tyuliev, An XPS study of thin NiO films deposited on MgO(100), Surf. Sci. 367 (1996) 196–202. doi:https://doi.org/10.1016/S0039-6028(96)00818-7.

[93] M.M. Zyryanova, P. V Snytnikov, R. V Gulyaev, Y.I. Amosov, A.I. Boronin, V.A. Sobyanin, Performance of Ni/CeO2 catalysts for selective CO methanation in hydrogen-rich gas, Chem. Eng. J. 238 (2014) 189–197. doi:https://doi.org/10.1016/j.cej.2013.07.034.

[94] X. Dong, B. Jin, Y. Sun, L. Yu, Urban gas production from low H2/CO biogas using Re-promoted Ni catalysts supported on modified manganese sand, Fuel. 220 (2018) 60–71. doi:https://doi.org/10.1016/j.fuel.2018.01.128.

[95] A.S. Al-Fatesh, M.A. Naeem, A.H. Fakeeha, A.E. Abasaeed, Role of La2O3 as Promoter and Support in Ni/γ-Al2O3 Catalysts for Dry Reforming of Methane, Chinese J. Chem. Eng. 22 (2014) 28–37. doi:https://doi.org/10.1016/S1004-9541(14)60029-X.

[96] I. Iglesias, A. Quindimil, F. Mariño, U. De-La-Torre, J.R. González-Velasco, Zr promotion effect in CO2 methanation over ceria supported nickel catalysts, Int. J. Hydrogen Energy. 44 (2019) 1710–1719. doi:https://doi.org/10.1016/j.ijhydene.2018.11.059.

[97] C. Mebrahtu, S. Abate, S. Perathoner, S. Chen, G. Centi, CO2 methanation over Ni catalysts based on ternary and quaternary mixed oxide: A comparison and analysis of the structure-activity relationships, Catal. Today. 304 (2018) 181–189. doi:https://doi.org/10.1016/j.cattod.2017.08.060.

[98] C. Fukuhara, K. Hayakawa, Y. Suzuki, W. Kawasaki, R. Watanabe, A novel nickel-based structured catalyst for CO2 methanation: A honeycomb-type Ni/CeO2 catalyst to transform greenhouse gas into useful resources, Appl. Catal. A Gen. 532 (2017) 12–18. doi:https://doi.org/10.1016/j.apcata.2016.11.036.

[99] L. Xu, H. Yang, M. Chen, F. Wang, D. Nie, L. Qi, X. Lian, H. Chen, M. Wu, CO2 methanation over Ca doped ordered mesoporous Ni-Al composite oxide catalysts: The promoting effect of basic modifier, J. CO2 Util. 21 (2017) 200–210. doi:https://doi.org/10.1016/j.jcou.2017.07.014.

[100] S. Takenaka, T. Shimizu, K. Otsuka, Complete removal of carbon monoxide in hydrogen-rich gas stream through methanation over supported metal catalysts, Int. J. Hydrogen Energy. 29 (2004) 1065–1073. doi:https://doi.org/10.1016/j.ijhydene.2003.10.009.

[101] M.A.A. Aziz, A.A. Jalil, S. Triwahyono, S.M. Sidik, Methanation of carbon dioxide on metal-promoted mesostructured silica nanoparticles, Appl. Catal. A Gen. 486 (2014) 115–122. doi:https://doi.org/10.1016/j.apcata.2014.08.022.

[102] M.A.A. Aziz, A.A. Jalil, S. Triwahyono, R.R. Mukti, Y.H. Taufiq-Yap, M.R. Sazegar, Highly active Ni-promoted mesostructured silica nanoparticles for CO2 methanation, Appl. Catal. B Environ. 147 (2014) 359–368. doi:https://doi.org/10.1016/j.apcatb.2013.09.015.

[103] B. Alrafei, I. Polaert, A. Ledoux, F. Azzolina-Jury, Remarkably stable and efficient Ni and Ni-Co catalysts for CO2 methanation, Catal. Today. (2019). doi:https://doi.org/10.1016/j.cattod.2019.03.026.

[104] W. Li, X. Nie, X. Jiang, A. Zhang, F. Ding, M. Liu, Z. Liu, X. Guo, C. Song, ZrO2 support imparts superior activity and stability of Co catalysts for CO2 methanation, Appl. Catal. B Environ. 220 (2018) 397–408. doi:https://doi.org/10.1016/j.apcatb.2017.08.048.

[105] D. Pandey, G. Deo, Effect of support on the catalytic activity of supported Ni–Fe catalysts for the CO2 methanation reaction, J. Ind. Eng. Chem. 33 (2016) 99–107. doi:https://doi.org/10.1016/j.jiec.2015.09.019.

[106] P. Panagiotopoulou, Hydrogenation of CO2 over supported noble metal catalysts, Appl. Catal. A Gen. 542 (2017) 63–70. doi:https://doi.org/10.1016/j.apcata.2017.05.026.

[107] A. Zhao, W. Ying, H. Zhang, H. Ma, D. Fang, Ni–Al2O3 catalysts prepared by solution combustion method for syngas methanation, Catal. Commun. 17 (2012) 34–38. doi:https://doi.org/10.1016/j.catcom.2011.10.010.

[108] J. Ashok, M.L. Ang, S. Kawi, Enhanced activity of CO2 methanation over Ni/CeO2-ZrO2 catalysts: Influence of preparation methods, Catal. Today. 281 (2017) 304–311. doi:https://doi.org/10.1016/j.cattod.2016.07.020.

Table 1. Physico-chemical features of the synthesized systems.

Sample	**L_{Ni}**[a] (wt.%)	**SA_{BET}** (m^2/g)	**PV_{BJH}**[b] ($cm^3 \cdot g^{-1}$)	**APD**[c] (nm)	**XRD**		**CO-Chemisorption**		**TEM**	**Band gap** (eV)
					Me_xO_y Lattice parameter[d] (nm)	Me_xO_y PS[d] (nm)	D_{Ni} (%)	PS_{Ni} (nm)	PS_{Ni} (nm)	
15Ni/CeO_2	15.1	20.6	0.065	12.6	0.538	10.4	5.2	19.1	*n.d.*	*n.d.*
15Ni/Al_2O_3	15.0	250.4	0.307	4.9	*n.d.*	*n.d.*	*n.d.*	*n.d.*	9.7	*n.d.*
Y_2O_3	-	35.9	0.262	29.2	1.060	13.5	-	-	-	5.78
7Ni/Y_2O_3	7.2	40.7	0.255	25.1	1.058 (1.052)	11.5 (12.7)	10.0	10.1	*n.d.*	5.65
15Ni/Y_2O_3	15.0	19.3	0.146	30.3	1.057 (1.055)	12.9 (13.5)	8.7	11.7	11.2	5.53
25Ni/Y_2O_3	25.1	20.7	0.183	35.4	1.057 (1.055)	11.3 (12.6)	7.3	13.9	12.1	5.01
35Ni/ Y_2O_3	34.8	26.9	0.163	24.2	1.057 (1.056)	8.8 (11.9)	4.1	24.8	*n.d.*	3.99

n.d. = not determined;

[a] *Nickel loading (L_{Ni}) determined by ICP/OES chemical analysis;*

[b] *BJH desorption cumulative Pore Volume in the range 1.7-300 nm;*

[c] *Average Pore Diameter from APD=4·PV/SA;*

[d] *Calculated from X-ray diffraction: lattice parameter by the relation* $\alpha = \sqrt{h^2 + k^2 + l^2} \cdot (\lambda/2 \cdot \sin\theta)$; *$CeO_2$ and Y_2O_3 size by the Scherrer's equation of the CeO_2 (111) and Y_2O_3 (222) reflections (in parentheses data obtained after catalyst reduction).*

Table 2. Experimental hydrogen consumption and reducibility from TPR profiles of the Ni-based catalysts.

Sample	**H_2 consumption**[a] (°C; $mmol_{H2}/g_{NiO}$)				**d_r**[b] (%)
	Low temperature peak	Medium temperature peak	High temperature peak	Total	
15Ni/CeO_2	270; 1.30	350; 8.75	440; 3.11	13.16	98.3
7Ni/Y_2O_3	200; 0.70	410; 6.26	500; 6.33	13.29	99.3
15Ni/Y_2O_3	210; 0.96	410; 5.56	505; 6.15	12.67	94.6
25Ni/Y_2O_3	240; 0.88	440; 4.47	515; 6.22	11.57	86.4
35Ni/ Y_2O_3	245; 0.54	460; 3.77	540; 6.53	10.84	81.0

[a] *Experimental H_2 consumption from ambient temperature to 600°C;*

[b] *Reduction degree of Nickel (d_r) calculated from the ratio between experimental and theoretical H_2 consumption. Theoretical H_2 consumption (13.39 $mmol_{H2}/g_{NiO}$) was determined by assuming complete reduction of NiO to Ni.*

Table 3. XPS analysis of the as-prepared and used catalysts: nature and surface distribution of Ni species.

Catalysts	As-prepared		Post-reacted	
	Ni(II) (at.%)	**Ni(II)* (at.%)**	**Ni(II) (at.%)**	**Ni^0 (at.%)**
15Ni/CeO_2	37	63	67	33
15Ni/Al_2O_3	100	-	100	-
7Ni/Y_2O_3	67	33	n.d.	n.d.
15Ni/Y_2O_3	44	56	32	68
25Ni/Y_2O_3	30	70	35 (39)[a]	65 (61)[a]
35Ni/ Y_2O_3	27	73	n.d.	n.d.

n.d. = not determined;

[a]In parentheses data obtained after 200 h stability test.

Table 4. CO_2-TPD analysis of the reduced catalysts: nature and distribution of basic sites.

Sample	CO_2 desorption ($\mu mol_{CO2}/g$)				Basic site density[a] ($\mu mol_{CO2}/m^2$)
	Weak (<150°C)	Moderate (150-450°C)	Strong (>450°C)	Total	
15Ni/CeO_2	11.87	2.89	41.60	56.36	2.74
15Ni/Al_2O_3	145.88	132.81	37.23	315.92	1.26
7Ni/Y_2O_3	69.66	74.08	10.70	154.44	3.79
15Ni/Y_2O_3	39.27	57.65	7.12	104.04	5.39
25Ni/Y_2O_3	48.39	64.22	18.05	130.66	6.31
35Ni/ Y_2O_3	54.58	109.82	24.06	188.46	7.01

[a]Expressed as total basic sites per unit surface area of catalyst.

Figure 1. Nitrogen adsorption-desorption isotherms (a,c) and pore size distributions (b,d) of synthesized systems.

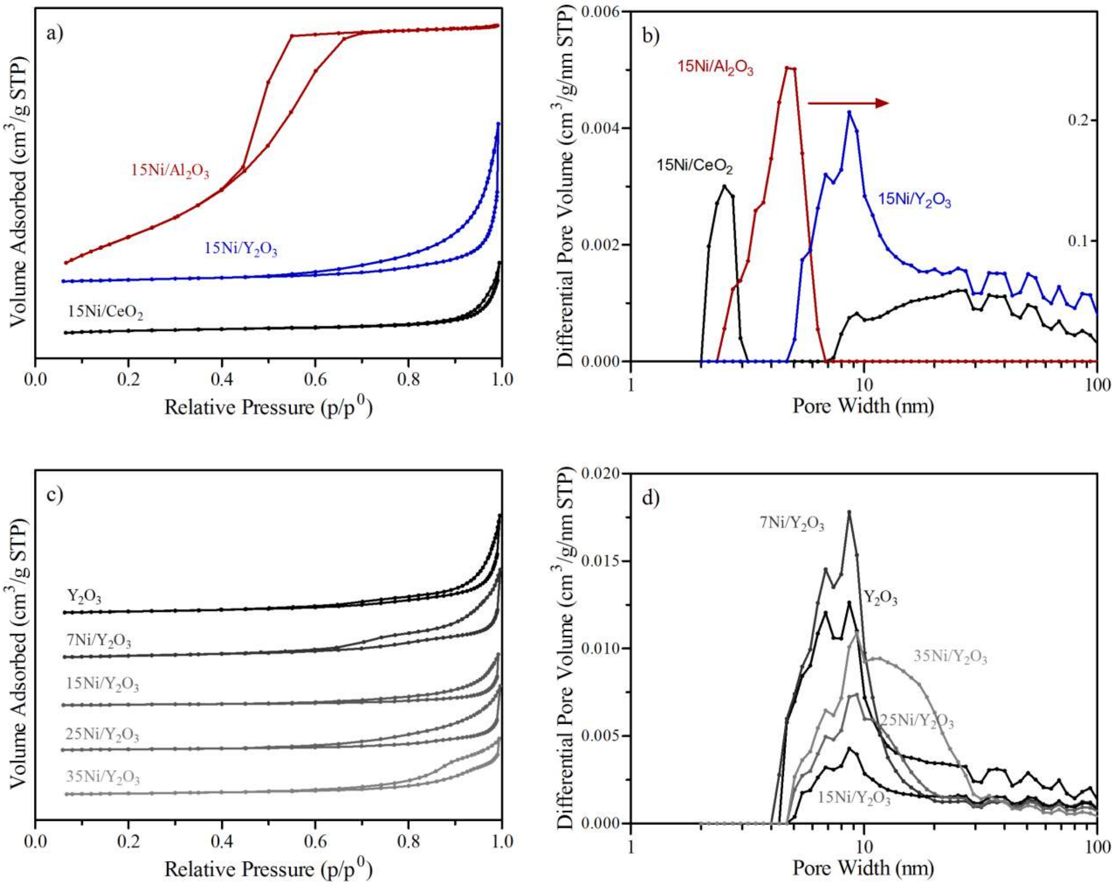

Figure 2. XRD patterns of Ni-based catalysts supported on CeO$_2$, Al$_2$O$_3$, and Y$_2$O$_3$ oxides (JCPDS reference peaks of NiAl$_2$O$_4$, Y$_2$O$_3$, CeO$_2$, and NiO also included).

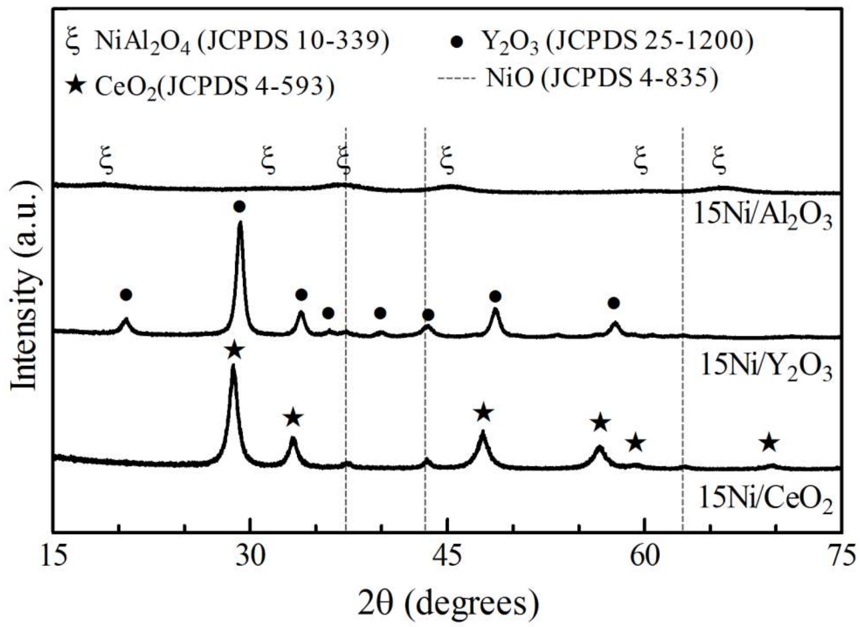

Figure 3. XRD patterns of as-prepared (a,b) and reduced (c,d) Ni/Y_2O_3 catalysts with different Ni loading (JCPDS reference peaks of NiO, Ni, and Y_2O_3 also included).

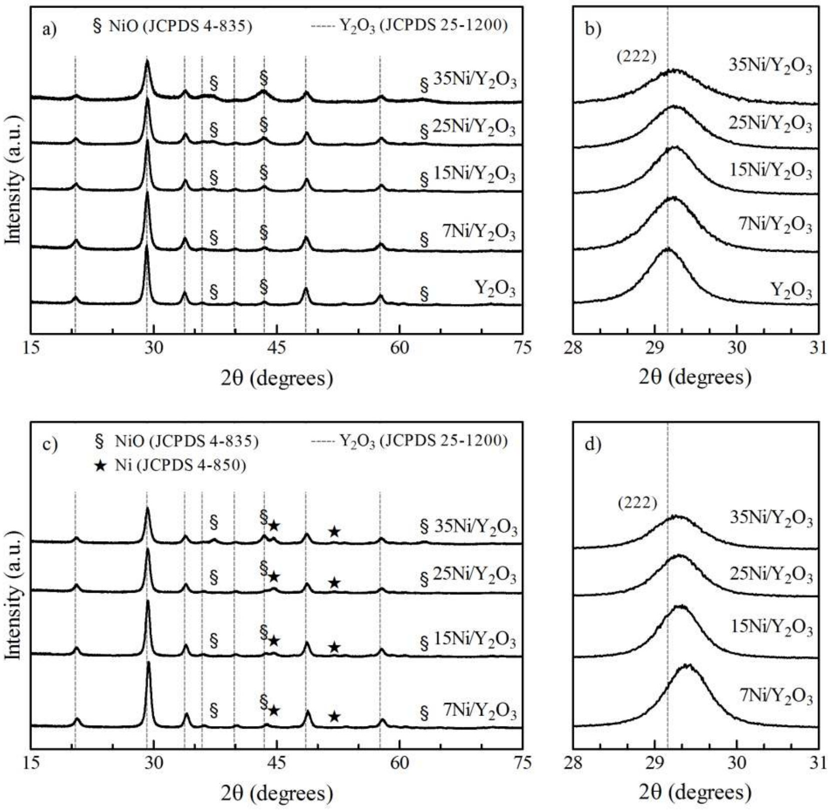

Figure 4. H_2-TPR profiles of synthesized catalysts: a) Ni-based catalysts supported on CeO_2, Al_2O_3, and Y_2O_3 oxides; b) Ni/Y_2O_3 catalysts with different Ni loading and corresponding Y_2O_3 support.

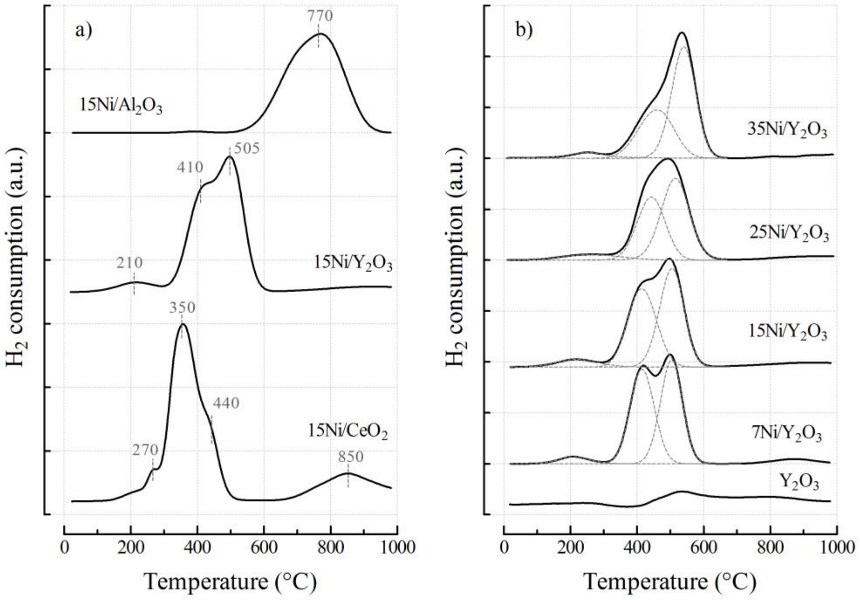

Figure 5. Representative TEM micrographs of reduced 15Ni/CeO_2 (a), 15Ni/Al_2O_3 (b), 15Ni/Y_2O_3 (c), 25Ni/Y_2O_3 (d,e), and 35Ni/Y_2O_3 (f) catalysts.

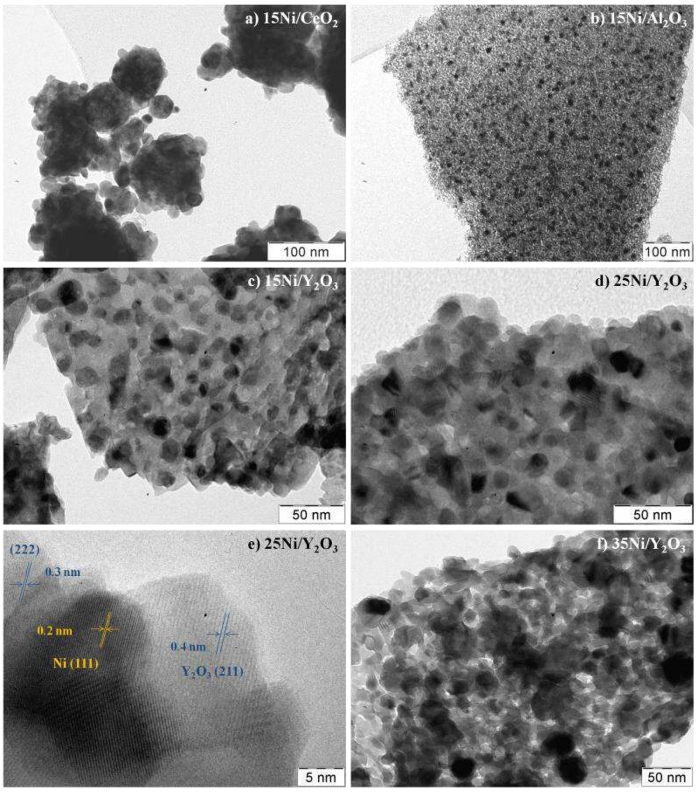

Figure 6. UV-Vis DRS spectra of Y_2O_3-based samples (a) and band gap estimation via Kubelka-Munk theory for Y_2O_3 support (b) and Ni/Y_2O_3 catalysts (c).

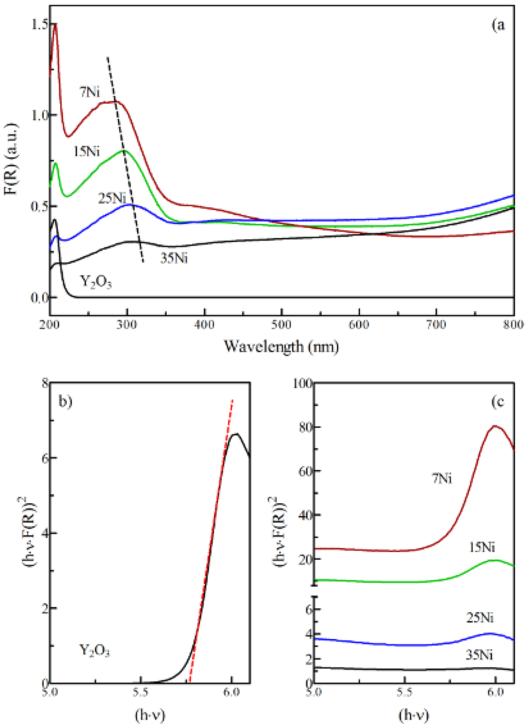

Figure 7. XPS analysis of as-prepared (a,b,c) and post-reacted (a,b,d) Ni/CeO$_2$ (a), Ni/Al$_2$O$_3$ (b), and Ni/Y$_2$O$_3$ (c,d) catalysts.

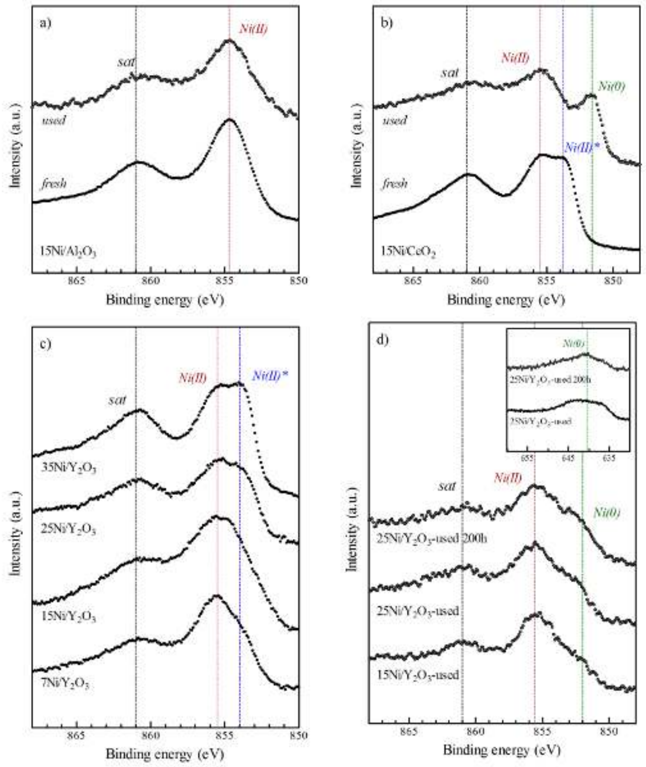

Figure 8. CO$_2$-TPD profiles of synthesized catalysts: a) Ni-based catalysts supported on CeO$_2$, Al$_2$O$_3$, and Y$_2$O$_3$ oxides; b) Ni/Y$_2$O$_3$ catalysts with different Ni loading.

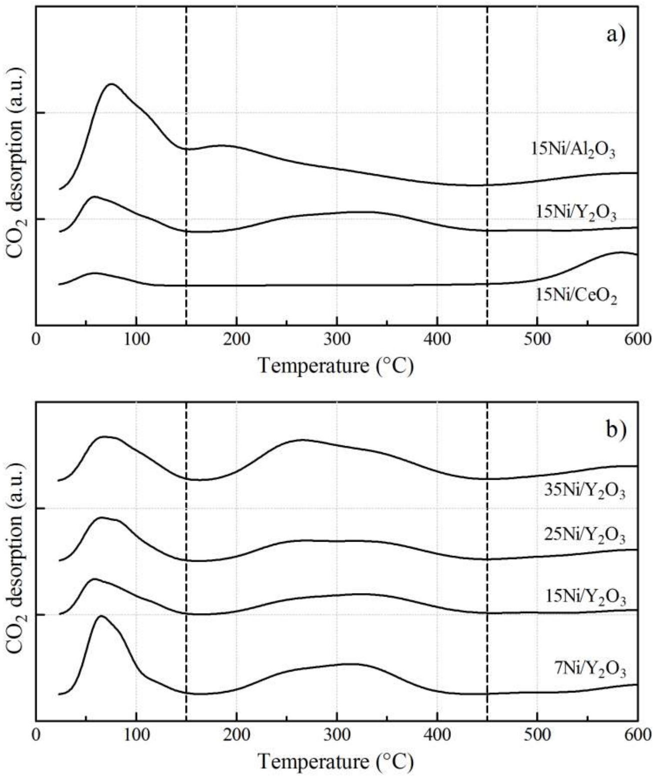

Figure 9. Light-off curves of Ni-based catalysts supported on CeO_2 (a), Al_2O_3 (b), and Y_2O_3 oxides (c). Activity parameters expressed as CO and CO_2 conversions and CH_4 yield. Experimental conditions: T = 250-500°C; GHSV = 10,000 h^{-1}, and $(H_2\text{-}CO_2)/(CO+CO_2) = 3$.

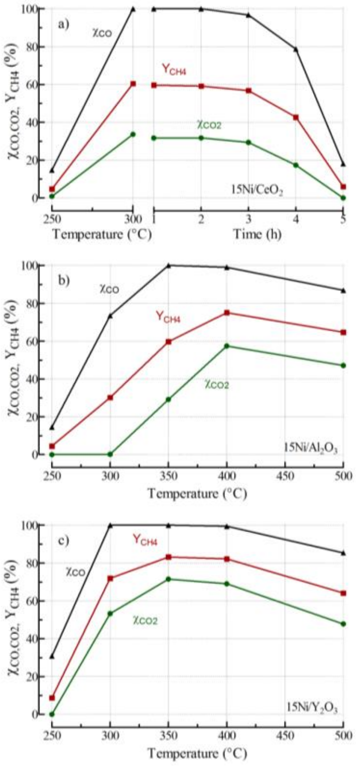

Figure 10. Light-off curves of Ni/Y_2O_3 catalysts with different Ni loading. Activity parameters expressed as CO conversion (a), CO_2 conversion (b), and CH_4 yield (c). Experimental conditions: T = 250-500°C; GHSV = 10,000 h^{-1}, and $(H_2\text{-}CO_2)/(CO+CO_2) = 3$.

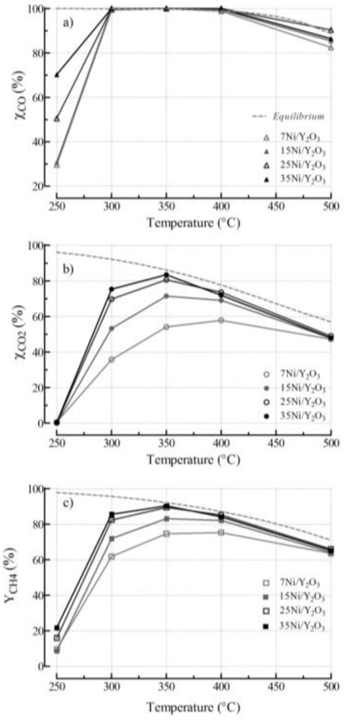

Figure 11. Representative TEM micrographs of post-reacted catalysts: 15Ni/CeO_2 (a-c), 15Ni/Al_2O_3 (d), and 15Ni/Y_2O_3 (e) after activity test; 25Ni/Y_2O_3 (f) after stability test.

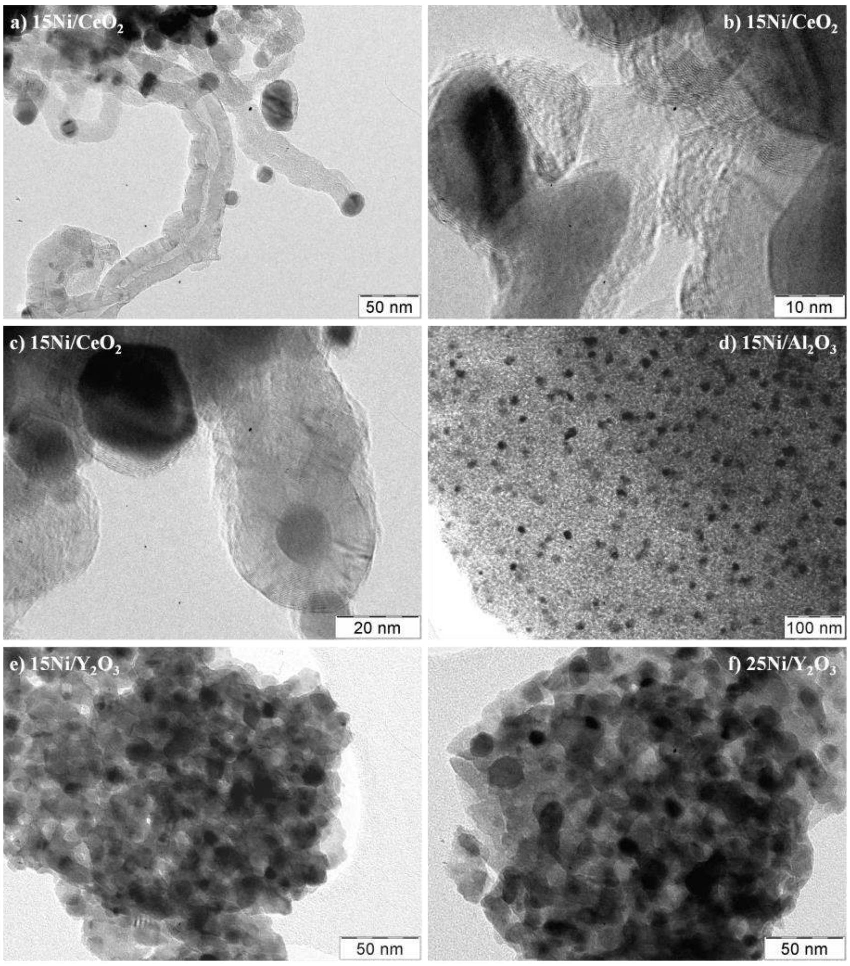

Figure 12. Effect of medium-strength basicity on the turnover frequency of CO_2 conversion over Ni/Y_2O_3 catalysts. Experimental conditions: T = 300°C; GHSV = 10,000 h^{-1}, and (H_2-CO_2)/(CO+CO_2) = 3.

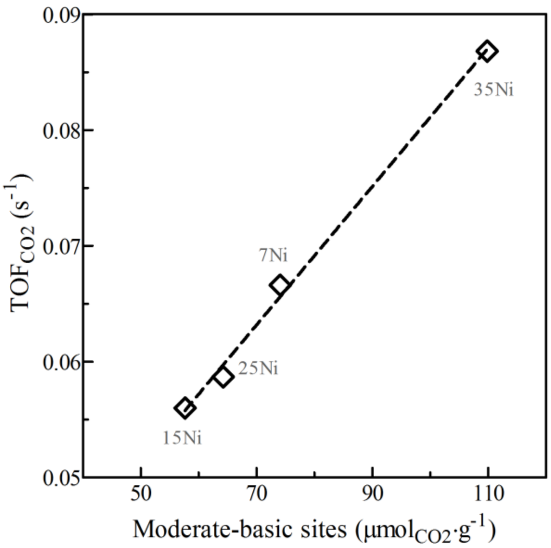

Figure 13. CO and CO_2 methanation stability over $25Ni/Y_2O_3$ catalyst. CO and CO_2 conversions and CH_4 as a function of time-on-stream. Experimental conditions: T = 350°C; GHSV = 10,000 h^{-1}, and $(H_2\text{-}CO_2)/(CO+CO_2) = 3$.